

Coexistence of Different Vacua in the Effective Quantum Field Theory and Multiple Point Principle[¶]

G. E. Volovik

Low Temperature Laboratory, Helsinki University of Technology, FIN-02015 HUT, Finland
Landau Institute for Theoretical Physics, Russian Academy of Sciences, Moscow, 117940 Russia

Received December 31, 2003

According to the Multiple Point Principle, our Universe is on the coexistence curve of two or more phases of the quantum vacuum. The coexistence of different quantum vacua can be regulated by the exchange of the global fermionic charges between the vacua, such as baryonic, leptonic, or family charge. If the coexistence is regulated by the baryonic charge, all the coexisting vacua exhibit the baryonic asymmetry. Due to the exchange of the baryonic charge between the vacuum and matter, which occurs above the electroweak transition, the baryonic asymmetry of the vacuum induces the baryonic asymmetry of matter in our Standard Model phase of the quantum vacuum. The present baryonic asymmetry of the Universe indicates that the characteristic energy scale, which regulates the equilibrium coexistence of different phases of quantum vacua, is about 10^6 GeV.
© 2004 MAIK “Nauka/Interperiodica”.

PACS numbers: 11.30.Fs; 12.10.Dm; 98.80.Cq; 64.10.+h

1. INTRODUCTION

Dealing with quantum vacuum whose “microscopic” physics is still unknown, the high-energy, general-relativity, and condensed-matter communities use different experience developed in working in each of those fields [1]. In condensed matter, there is a rather general class of fermionic systems, where the relativistic quantum field theory gradually emerges at low energy and where the momentum-space topology is responsible for the mass protection for fermions, so that masses of all the fermions are much smaller than the natural energy scale provided by the microscopic (trans-Planckian) physics [2]. Since the vacuum of the Standard Model belongs to the same universality class of quantum vacua, this condensed-matter example provides us with some criteria for selection of the particle physics theories: the theory which incorporates the Standard Model must be consistent with its condensed-matter analogue.

Here, we apply such criteria to the Multiple Point Principle (MPP) [3–6]. According to MPP, nature chooses the parameters of the Standard Model such that two or several phases of the quantum vacua have the same energy density. These phases coexist in our Universe in the same manner as different phases of quantum liquids, such as superfluid phases A and B of ^3He or mixtures of ^3He and ^4He liquids. Using MPP, Nielsen and coworkers arrived at some prediction for the correlation between the fine structure constants in their extension of the Standard Model. The fine tuning of the

coupling constants is similar to the fine tuning of the chemical potentials of the coexisting quantum liquids in equilibrium.

The problem of the Standard Model parameters is thus related to the problem of the vacuum energy and, correspondingly, to the cosmological constant problem. It was suggested [6] that MPP can serve as a basic principle to explain the present value of the cosmological constant. From the condensed-matter point of view, such connection is rather natural. According to observations, the cosmological constant is (approximately) zero in our phase of the quantum vacuum, which is why it must be (almost) zero in all the coexisting vacua as well. In condensed matter, such nullification of the vacuum energy occurs for the arbitrary phase of the quantum vacuum. This happens due to the thermodynamic Gibbs–Duhem relation, according to which the microscopic (trans-Planckian) degrees of freedom exactly cancel the contribution to the vacuum energy from the low-energy (sub-Planckian) degrees of freedom [2]. The phenomenon of nullification is so general that it must be applicable to any macroscopic system including the quantum vacuum of relativistic quantum fields, irrespective of whether the vacuum is true or false, and even if we do not know the microscopic physics.

Since the MPP is justified by the condensed-matter analogue, we can apply it to different problems related to quantum vacuum. Here, we discuss the scenario of the baryonic asymmetry of the Universe, which follows from MPP.

[¶]This article was submitted by the author in English.

2. ADJUSTMENT OF THE QUANTUM VACUUM AFTER PHASE TRANSITION

The phase transitions between different quantum vacua does not influence the phenomenon of nullification of the vacuum energy: the energies of the vacuum are zero both above the transition and also after some transient period below the phase transition. In quantum liquids, the microscopic degrees of freedom, which adjust themselves to nullify the energy density in a global equilibrium, are the underlying bare particles—atoms of the liquid. The number density n of atoms changes after the phase transition, and this compensates the change of the vacuum energy. For example, after the phase transition between superfluid $^3\text{He-A}$ and superfluid $^3\text{He-B}$, the relative change in the particle density is

$$\frac{\delta n}{n} \sim \frac{T_c^2}{E_F^2}. \quad (1)$$

Here, the superfluid transition temperature T_c characterizes the energy scale of the superfluid phase transition and also the transition between $^3\text{He-A}$ and $^3\text{He-B}$; the Fermi energy $E_F \gg T_c$ characterizes the atomic (Planck) energy scale of the liquid. It is important that the correction to the microscopic parameter n (and also to E_F : $\delta E_F/E_F \sim \delta n/n$) is very small, and, thus, it does not influence the parameters of the effective theory of superfluidity in the low-energy corner.

The translation to the language of the Standard Model is almost straightforward. Let us consider the relative change of the microscopic (trans-Planckian) parameters needed to nullify the vacuum energy of the Standard Model after, say, the electroweak phase transition. In this case, one must identify $T_c \equiv E_{\text{ew}}$ and $E_F \equiv E_{\text{Pl}}$ (the Planck energy). The relative change of the microscopic parameters in quantum liquids corresponds to the relative change of the Planck physics parameters, and, thus, one can identify $\delta n/n \equiv \delta E_{\text{Pl}}/E_{\text{Pl}}$. However, Eq. (1) is not applicable for the Standard Model. The reason is that the fermionic density of states (DOS) in the Standard Model above the electroweak phase transition differs from the DOS in liquid ^3He above the superfluid phase transition. The vacuum in nonsuperfluid normal ^3He above the superfluid transition belongs to the Fermi-surface universality class, while the vacuum of the Standard Model above the electroweak transition belongs to the universality class with Fermi points. That is why they have different density of fermionic states: $N(E) \rightarrow \text{const} \sim E_F^2 \equiv E_{\text{Pl}}^2$ in the vicinity of the Fermi surface and $N(E) \rightarrow E^2$ in the vicinity of the Fermi point. Thus, the energy density related to superfluidity is $T_c^2 N(E = T_c) \sim T_c^2 E_{\text{Pl}}^2$, while the energy density involved in the electroweak transition is $E_{\text{ew}}^2 N(E = E_{\text{ew}}) \sim E_{\text{ew}}^4$. This gives an additional factor $E_{\text{ew}}^2/E_{\text{Pl}}^2$; as a result, the relative correction to the

Planck energy needed to compensate the energy change of the vacuum after the electroweak transition is

$$\frac{\delta E_{\text{Pl}}}{E_{\text{Pl}}} \sim \frac{E_{\text{ew}}^4}{E_{\text{Pl}}^4}. \quad (2)$$

Such response of the vacuum is so extremely small that it cannot influence the parameters of the effective low-energy theory, the Standard Model.

This demonstrates that the adjustment of the deep vacuum does not lead to any sizable correlation between the parameters of the Standard Model, and, thus, the cosmological constant problem has nothing to do with the parameters of the effective theory. However, the MPP contains a stronger assumption than the statement that each vacuum always acquires zero energy. It assumes that several essentially different vacua have zero energy simultaneously, i.e., these vacua coexist in the same Universe (though the phase boundaries between different vacua can be well beyond the cosmological horizon). The coexistence, though it does not influence the parameters of the effective theories, leads to other physical consequences, such as baryonic asymmetry of the Universe. Let us discuss the principles of the coexistence of quantum vacua using as an example the coexisting quantum liquids, where the coexistence can be regulated by both microscopic and macroscopic parameters (analogues of microscopic or macroscopic fermionic charges).

3. COEXISTING VACUA

Let us first consider the quantum liquid formed by the mixture of k sorts of atoms. An example of the mixture of $k = 2$ components is provided by the liquid solution of ^3He atoms in ^4He liquid. The number of atoms N_a of each species a is conserved, and it serves as the conserved microscopic fermionic charge of the vacuum (the ground state of the mixture). The relevant vacuum energy whose gradient expansion gives rise to the effective quantum field theory for quasiparticles at low energy is [7]

$$\rho_{\text{vac}} = \frac{1}{V} \left\langle \mathcal{H} - \sum_{a=1}^k \mu_a \mathcal{N}_a \right\rangle_{\text{vac}}, \quad (3)$$

where \mathcal{H} is the Hamiltonian of the system, \mathcal{N}_a is the particle number operator for atoms of sort a in the mixture, and μ_a is their chemical potential. If the liquid is in equilibrium, it obeys the Gibbs–Duhem relation, which expresses the energy $E = \langle \mathcal{H} \rangle$ through the other thermodynamic variables, including the temperature T , the entropy S , the particle number $N_a = \langle \mathcal{N}_a \rangle$, and the pressure P :

$$E - TS - \sum_{a=1}^k \mu_a N_a = -PV. \quad (4)$$

From this thermodynamic relation and Eq. (3), one obtains at $T = 0$ the familiar equation of state for the vacuum, which is valid both for relativistic and nonrelativistic systems:

$$\rho_{\text{vac}} = \epsilon - \sum_{a=1}^k \mu_a n_a \equiv \frac{1}{V} \left(E - \sum_{a=1}^k \mu_a N_a \right) = -P, \quad (5)$$

where we also introduced the energy density $\epsilon = E/V$ and particle number density $n_a = N_a/V$.

If the system is isolated from the environment, its pressure is zero and, thus, the energy density is zero too:

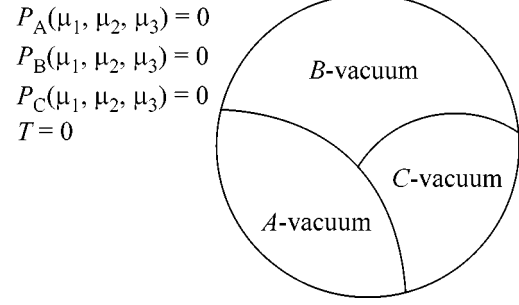
$$\rho_{\text{vac}} = -P = 0. \quad (6)$$

For such condensed-matter systems, in which the effective gravity emerges in the low-energy corner, this equation means that the effective cosmological constant is zero. This nullification occurs without fine tuning for any vacuum since the microscopic degrees of freedom (the particle number densities n_a and chemical potentials μ_a) automatically adjust themselves in equilibrium in such a way that the Gibbs–Duhem relation (4) is satisfied.

The more components the liquid has, the more flexible the vacuum state is, and, as a result, the number ν of different vacua which can coexist is bigger. In such flexible system, the Multiple Point Principle naturally emerges. For the system with k components, the maximal number of different vacua which can coexist being separated by the phase boundaries is $\nu_{\text{max}} = k$ (see the figure for $\nu = k = 3$), and all of these vacua have zero energy density: $\rho_{\text{vac}}^i = 0$ ($i = 1, \dots, \nu_{\text{max}}$). This results from the following consideration. The coexisting vacua must have the same chemical potentials μ_a because of the exchange of particles between the vacua. They also have the same pressure $P = 0$ (and the same temperature $T = 0$). Thus, for each vacuum i , the pressure as a function of the chemical potentials must be zero: $P^{(i)}(\mu_1, \mu_2, \dots, \mu_k) = 0$. All these ν equations can be satisfied simultaneously if $\nu \leq k$. This is the conventional phase rule [8] which is constrained by the condition that two thermodynamic variables are fixed, $P = 0$ and $T = 0$.

4. COEXISTENCE OF VACUA REGULATED BY EFFECTIVE FERMIONIC CHARGES

Does the coexistence of quantum vacua lead to observable consequences for the effective field theories emerging in these vacua? The answer is yes if some of the variables n_a are soft variables belonging to the low-energy world, such as the density of the baryonic charge stored in the vacuum. An example is provided by the superfluid phases of ^3He , A and B, which can



Example of $\nu = 3$ coexisting vacua A, B, and C in a droplet of a substance with $k = 3$ conserved charges, N_1, N_2 , and N_3 . The droplet is isolated from the environment, so that, in all three vacua, the pressure $P = 0$ if the curvature of the boundary of the droplet and the curvature of interfaces are neglected. That is why the energy density is also zero in all three coexisting vacua: $\rho_A = \rho_B = \rho_C = 0$. Volumes V_A, V_B , and V_C occupied by the three vacua are determined by the total microscopic fermionic charges of the droplet: the particle numbers $N_1 = V_A n_{1A} + V_B n_{1B} + V_C n_{1C}$, $N_2 = V_A n_{2A} + V_B n_{2B} + V_C n_{2C}$, and $N_3 = V_A n_{3A} + V_B n_{3B} + V_C n_{3C}$.

coexist at $T = 0$ and $P = 0$ in an applied magnetic field \mathbf{H} [9]. The corresponding vacuum energy density is

$$\rho_{\text{vac}} = \epsilon - \mu n - \Omega \cdot \mathbf{S}, \quad (7)$$

where n is the number density of ^3He atoms, \mathbf{S} is the density of the angular momentum which comes from the spins of the atoms (each atom has spin $\hbar/2$), $\Omega = \gamma \mathbf{H}$, and γ is the gyromagnetic ratio of the ^3He atom. For a given direction of the magnetic field, say, $\mathbf{H} = H \hat{z}$, the liquid can be represented as the mixture of the $k = 2$ components, with spin up and spin down:

$$\rho_{\text{vac}} = \epsilon - \mu_{\uparrow} n_{\uparrow} - \mu_{\downarrow} n_{\downarrow}, \quad (8)$$

where

$$n_{\uparrow} = \frac{n}{2} + \frac{S_z}{\hbar}, \quad n_{\downarrow} = \frac{n}{2} - \frac{S_z}{\hbar}, \quad (9)$$

$$\mu_{\uparrow} = \mu + \frac{\hbar}{2} \Omega, \quad \mu_{\downarrow} = \mu - \frac{\hbar}{2} \Omega.$$

Since we have effectively $k = 2$ components, the $\nu = 2$ vacua can coexist in the absence of the environment, i.e., at $P = 0$. This is the reason why A and B phases can coexist at $T = 0$ and $P = 0$.

Unlike the variable n , the fermionic charge S_z is a soft variable since, in typical situations, it is zero (in the absence of external magnetic field). When the two vacua coexist, both variables n and S_z adjust themselves to nullify the pressure (and, thus, to nullify the ‘‘cosmological constant’’ ρ_{vac}) in each of the two phases. However, while the change of the particle density is negligibly small, $\delta n/n \propto T_c^2/E_F^2 \ll 1$, the change of the variable S_z is substantial since it changes from zero. The energy density related to nonzero S_z is on the order of

S_z^2/E_{Pl}^2 . Comparing this with the superfluid energy $T_c^2 E_{\text{Pl}}^2$, one finds that the characteristic spin density of the vacuum which emerges to compensate the AB phase transition is

$$|n_{\uparrow} - n_{\downarrow}| \sim T_c E_{\text{Pl}}^2, \quad \left| \frac{n_{\uparrow} - n_{\downarrow}}{n_{\uparrow} + n_{\downarrow}} \right| \sim \frac{T_c}{E_{\text{Pl}}}. \quad (10)$$

This is much bigger than the relative change in the particle density n after adjustment in Eq. (1). As a result, the parameters of the effective theory, which describe superfluidity, also change considerably. In particular, the originally isotropic B phase becomes highly anisotropic in the applied magnetic field (or at nonzero spin density of the liquid) needed for coexistence of A and B phases.

Note that S_z is the fermionic charge of the vacuum, and, in principle, it is not related to the fermionic charge of matter, since, in our example, the matter (quasiparticles) is absent. However, the charge asymmetry in the vacuum sector can cause the charge asymmetry in the matter sector due to exchange between the vacuum and matter. The resulting excess of the fermionic charge in the matter sector can induce the nonzero matter density even at $T = 0$. This is similar to the nonzero matter density in our Universe caused by the baryonic asymmetry of matter. Let us consider how this baryonic charge can be induced.

5. COEXISTENCE AND THE BARYONIC ASYMMETRY OF THE VACUUM

Let us start with the baryonic charge of the vacuum of the relativistic quantum field exploiting an analogy between the macroscopic global charges: the spin S_z of the quantum liquid in its ground state and the global charges in our quantum vacuum, such as the baryonic charge B (or the family charge F [10]). The spin S_z of the liquid must be nonzero to provide the coexistence of the A and B vacua in superfluid ^3He at $T = 0$. In the same manner, the baryonic charge B or family charge F could naturally arise in the quantum vacuum to establish the equilibrium between the coexisting phases of the vacuum.

Let us consider the coexistence of several vacua whose physics differ below the energy scale $E_{ce} \ll E_{\text{Pl}}$. Such vacua can result from the broken symmetry phase transition, which occurs at $T \sim E_{ce}$, and we assume that the ordered phases differ by their residual symmetries H . The energy densities involved in the coexistence of the vacua are on the order of E_{ce}^4 . Let us assume that the coexistence is regulated by the exchange of the baryonic charge between the vacua. Then, one can estimate the density of this baryonic charge in the vacua by equating the energy density difference E_{ce}^4 and the energy density of the vacuum due to the nonzero charge

density B . If the baryonic charge is stored in the microscopic degrees of freedom of the quantum vacuum, the energy density related to this charge must be on the order of B^2/E_{Pl}^2 . As a result, the baryonic charge density of the vacuum needed for the coexistence of different vacua is

$$B_{\text{vac}} \sim E_{ce}^2 E_{\text{Pl}}. \quad (11)$$

Thus, the coexistence results in the baryonic asymmetry in the vacuum sector. In turn, the nonzero baryonic charge of the vacuum could be in the origin of the baryonic asymmetry of the matter in our Universe—an excess of the baryons over antibaryons, $n_B > n_{\bar{B}}$. Let us consider this mechanism of baryogenesis.

6. FROM BARYONIC ASYMMETRY OF THE VACUUM TO BARYONIC ASYMMETRY OF THE UNIVERSE

If an exchange of the baryonic charge between the vacuum and matter is possible, the chemical potential for the baryons in matter must be equal to the chemical potential for the baryonic charge in the vacuum. The latter is nonzero due to the nonzero baryonic charge in the vacuum sector in Eq. (11):

$$\mu_B \sim \frac{B_{\text{vac}}}{E_{\text{Pl}}^2} \sim \frac{E_{ce}^2}{E_{\text{Pl}}}. \quad (12)$$

At temperature $T \gg \mu_B$, one obtains the following estimation for the baryonic charge stored in the matter sector (in the gas of relativistic fermions):

$$B_{\text{matter}} = n_B - n_{\bar{B}} \sim T^2 \mu_B \sim \frac{T^2 E_{ce}^2}{E_{\text{Pl}}}. \quad (13)$$

However, the exchange between the vacuum and matter occurs (due to axial anomaly) only at T above the electroweak transition, $T > E_{\text{ew}}$. Below the transition, at $T < E_{\text{ew}}$, the exchange with the quantum vacuum is highly suppressed: the transition rate due to the sphaleron mechanism becomes exponentially weak [11, 12]. At the moment of the phase transition, i.e., at $T \sim E_{\text{ew}}$, the baryonic asymmetry of matter (primordial baryon-to-entropy ratio) is

$$\eta = \frac{n_B - n_{\bar{B}}}{s} \sim \frac{T^2 \mu_B}{T^3} \sim \frac{E_{ce}^2}{E_{\text{ew}} E_{\text{Pl}}}. \quad (14)$$

Below the transition, the baryonic charge in the matter sector is completely separated from the vacuum and evolves together with matter, while the density of the baryonic charge in the vacuum sector remains constant.

In the matter sector, the baryonic density evolves in the same way as the entropy and, thus, the baryon-to-entropy ratio η remains the same as at the moment of transition. To obtain the value $\eta \sim 10^{-10}$, which follows

from the cosmological observations [11, 12], the characteristic energy \bar{E}_{ce} , related to the baryonic charge of the vacuum, must be

$$E_{ce} \sim 10^{-5} \sqrt{E_{ew} E_{Pl}} \sim 10^6 \text{ GeV}. \quad (15)$$

In analogy with A and B phases of ${}^3\text{He}$, this corresponds to the transition temperature T_c at which the coexisting vacua were formed due to symmetry breaking.

The main point in this scenario of the baryogenesis is that the vacuum and matter are two subsystems, whose properties related to the fermionic (baryonic) charge are different. In condensed matter, the analogous exchange of spin charge between the superfluid vacuum and quasiparticles (matter) plays an important role in the spin dynamics of the system (see [13] and Section 8.6 in [9]).

7. CONCLUSIONS

In conclusion, the gravitating part of the vacuum energy is always zero in equilibrium vacuum, $\rho_{vac} = 0$, even if the cosmological phase transition occurs. The nullification after the phase transition is supported by automatic adjustment of the microscopic ultraviolet degrees of freedom. However, because of the huge energy stored in the microscopic degrees, the relative change in the microscopic parameters is extremely small, and this adjustment practically does not influence the parameters of the effective infrared theories. As a result, the Multiple Point Principle, which implies the coexistence of two or several different (i.e., not connected by symmetry) vacua, naturally occurs, and all the coexisting vacua automatically acquire zero energy without any fine tuning.

If the Universe is on the coexistence curve, this may lead to the observable physical consequences related to the fermionic charges of the vacuum and matter. In particular, if the coexistence is regulated by the exchange

of the baryonic charge, all the coexisting vacua acquire the baryonic asymmetry. The latter in turn gives rise to the baryonic asymmetry in the matter sector.

According to Eqs. (15) and (11), the density of the baryonic charge in the vacuum sector is rather high, $B_{vac} \sim 10^{-26} E_{Pl}^3$. What are the consequences of such CP violation in the quantum vacuum is the subject of further investigations.

I thank A.F. Andreev for illuminating discussion. This work was supported by ESF COSLAB Program and by the Russian Foundation for Basic Research.

REFERENCES

1. Giovanni Amelino-Camelia, gr-qc/0309054.
2. G. E. Volovik, *The Universe in a Helium Droplet* (Clarendon, Oxford, 2003).
3. D. L. Bennett, C. D. Froggatt, and H. B. Nielsen, in *Proceedings of the 27th International Conference on High Energy Physics*, Ed. by P. Bussey and I. Knowles (IOP, 1995), p. 557.
4. C. D. Froggatt, hep-ph/0312220.
5. C. D. Froggatt and H. B. Nielsen, hep-ph/0308144.
6. C. Froggatt, L. Laperashvili, R. Nevzorov, and H. B. Nielsen, hep-ph/0310127.
7. A. A. Abrikosov, L. P. Gor'kov, and I. E. Dzyaloshinskiĭ, *Quantum Field Theoretical Methods in Statistical Physics* (Fizmatgiz, Moscow, 1962; Pergamon, Oxford, 1965).
8. E. M. Lifshits and L. P. Pitaevskiĭ, *Course of Theoretical Physics*, Vol. 5: *Statistical Physics* (Nauka, Moscow, 1978; Pergamon, New York, 1980).
9. D. Vollhardt and P. Wölfle, *The Superfluid Phases of Helium 3* (Taylor and Francis, London, 1990).
10. G. E. Volovik, JETP Lett. **78**, 691 (2003).
11. M. Dine and A. Kusenko, Rev. Mod. Phys. **76**, 1 (2004).
12. M. Trodden, Rev. Mod. Phys. **71**, 1463 (1999).
13. A. J. Leggett and S. Takagi, Phys. Rev. Lett. **34**, 1424 (1975); Ann. Phys. (N.Y.) **106**, 79 (1977).

New Limits on Dinucleon Decay into Invisible Channels[†]

V. I. Tretyak*, V. Yu. Denisov, and Yu. G. Zdesenko

Institute for Nuclear Research, Kiev, 03680 Ukraine

*e-mail: tretyak@kinr.kiev.ua

Received December 16, 2003

Data of the radiochemical experiment (E.L. Fireman, 1978) with 1.7 t of $\text{KC}_2\text{H}_3\text{O}_2$, accumulated deep underground during ≈ 1 yr, were reanalyzed to set limits on dinucleon (nn and np) decays into invisible channels (disappearance, decay into neutrinos, etc.). The obtained lifetime bounds $\tau_{np} > 2.1 \times 10^{25}$ yr and $\tau_{nn} > 4.2 \times 10^{25}$ yr (at 90% C.L.) are better (or competitive) than those established in the recent experiments. © 2004 MAIK “Nauka/Interperiodica”.

PACS numbers: 13.30.-a; 14.20.Dh

The more than three-decade-long searches for proton decay, which is predicted by the Grand Unified Theories, continue to be one of the most important and intriguing subjects in the quest for effects beyond the Standard Model of elementary particles [1]. Up to now, only lifetime limits were established for such processes, being on the level of $\tau > 10^{30}$ – 10^{33} yr for nucleon decay into particles, which can strongly or electromagnetically interact with the nuclei contained in the detector's sensitive volume [2]. Recently, interest has increased in nucleon decays into so-called “invisible” channels (which are complementary to conventional ones [2]), when a nucleon or pair of nucleons decay into some weakly interacting particles (for example, neutrinos) or disappear. The last possibility is related with theories describing our world as four-dimensional brane embedded in a higher-dimensional structure [3–5]. According to [5], the disappearance of particles into extra dimensions is a generic property of matter. Searches for disappeared energy and/or momentum in particles' collision are planned with accelerators at high energies [6]. An experiment to search for the disappearance of orthopositronium is discussed in [7]. Perspectives to search for invisible decays of neutrons and dineutrons in ^{12}C with the 1000 t KamLAND detector are examined in [8], and sensitivities of future a 1000-t lead perchlorate detector for n disappearance in ^{35}Cl and ^{208}Pb are considered in [9].

As for the to-date status, the most stringent limits for nucleon and dinucleon decay into invisible channels have been known from the experiments performed during few last years (all bounds are given with 90% C.L.):

(1) $\tau_p > 3.5 \times 10^{28}$ yr—from the number of free neutrons which could be created as a result of p disappearance in deuterium nuclei ($d = pn$), which are contained in 1000 t of D_2O of the SNO apparatus [10];

(2) $\tau_p > 3.9 \times 10^{29}$ yr and $\tau_n > 3.9 \times 10^{29}$ yr—from the number of γ quanta with $E_\gamma = 6$ – 7 MeV which will be emitted in deexcitation of ^{15}O or ^{15}N after n or p disappearance in ^{16}O nucleus in 1000 t of the SNO heavy water [11];

(3) $\tau_{pp} > 5.0 \times 10^{25}$ yr and $\tau_{nn} > 4.9 \times 10^{25}$ yr—from the search for decay of radioactive nuclei (^{10}C , ^{11}Be , and ^{14}O) created after pp and nn disappearance in ^{12}C , ^{13}C , and ^{16}O nuclei in liquid scintillator (4.2 t of $\text{C}_{16}\text{H}_{18}$) and water shield (1000 t) of the BOREXINO Counting Test Facility [12];

(4) $\tau_{np} > 3.2 \times 10^{23}$ yr—from the search for decay of ^{134}I created as a result of np disappearance in ^{136}Xe [13].

In order to improve the τ_{np} limit, we reanalyze here the data of the old radiochemical experiment [14] where the daughter nuclide ^{37}Ar was searched for as a possible product of the p or n disappearance in ^{39}K . The target, 1710 kg of potassium acetate $\text{KC}_2\text{H}_3\text{O}_2$, which contains 9.7×10^{27} atoms of ^{39}K , was exposed deep underground (the Homestake mine, 4400 m w.e.) for more than 1 yr. The production rate of ^{37}Ar , extracted from the target and detected due to its radioactive decay $^{37}\text{Ar} \rightarrow ^{37}\text{Cl}$ ($T_{1/2} = 35$ days), for the last 3.5-month period was measured as 0.3 ± 0.6 atom/day. On this basis, the authors of [14, 15] have accepted the limit on the production rate of ^{37}Ar as 1 atom/day and have calculated the restrictions on the p and n lifetimes. For example, after the p decay in ^{39}K , the nucleus ^{38}Ar will be created, as a rule being in an excited state (unless the disappeared p was on the outermost shell). The authors estimated that, in 22.2% of cases, an additional neutron will be emitted from ^{38}Ar in the deexcitation process, giving rise to an ^{37}Ar nucleus [14, 15]. Similarly, after

[†]This article was submitted by the authors in English.

the n disappearance in initial ${}^{39}_{19}\text{K}$, produced ${}^{38}_{19}\text{K}$ emits p with a 20.4% probability, which will also result in the ${}^{37}_{18}\text{Ar}$ nucleus. From these values, accounting for 19 protons and 20 neutrons in the ${}^{39}_{19}\text{K}$, the limits $\tau_p = \tau_n = 1.1 \times 10^{26}$ yr were set [14, 15].

However, the same data can be used to calculate the τ_{np} limit, just noticing that the simultaneous disappearance of the np pair in ${}^{39}_{19}\text{K}$ also will produce the ${}^{37}_{18}\text{Ar}$ nucleus. The corresponding limit on the lifetime can be derived by using the formula

$$\lim \tau = N_{\text{nuc1}} \times N_{\text{obj}}^{\text{eff}} \times t / \lim S, \quad (1)$$

where N_{nuc1} is the number of ${}^{39}\text{K}$ nuclei, $N_{\text{obj}}^{\text{eff}}$ is the “effective” number of objects (here, np pairs) whose disappearance in the parent nucleus will result in the creation of the daughter nuclide, t is the time of measurements, and $\lim S$ is the number of effect’s events which can be excluded at a given confidence level on the basis of the experimental data.

According to the Feldman–Cousins procedure [2, 16], the measured value of the ${}^{37}\text{K}$ production rate $S/t = 0.3 \pm 0.6$ atom/day results in the limit $\lim S/t = 1.28$ atom/day at 90% C.L. Conservatively, supposing only *one* np pair (for one unpaired proton in the ${}^{39}_{19}\text{K}$ nucleus; disappearance of the outermost proton and neutron on the nucleons shell in the parent nucleus will produce a daughter in a nonexcited state) and using Eq. (1) with $N_{\text{nuc1}} = 9.7 \times 10^{27}$, we obtain the following np lifetime limit:

$$\lim \tau_{np} = 2.1 \times 10^{25} \text{ yr at 90\% C.L.}$$

In addition, the τ_{nn} bound can also be determined: the disappearance of the nn pair from ${}^{39}_{19}\text{K}$ nucleus will give ${}^{37}_{19}\text{K}$, which quickly decays again to ${}^{37}_{18}\text{Ar}$ with $T_{1/2} = 1.2$ s [17].¹ The number of objects, $N_{\text{obj}}^{\text{eff}}$, can be calculated in the following way [12, 18, 19]. After the disappearance of neutrons with binding energies $E_{n1}^b(A, Z)$ and $E_{n2}^b(A, Z)$ in (A, Z) nucleus, the excitation energy of the $(A - 2, Z)$ daughter, E_{exc} , can be approximated as $E_{\text{exc}} = E_{n1}^b(A, Z) + E_{n2}^b(A, Z) - 2S_n(A, Z)$, where $S_n(A, Z)$ is the binding energy of the least bound neutron in the (A, Z) nucleus. In the process of deexcitation of the $(A - 2, Z)$ daughter, only γ quanta can be emitted when the value of E_{exc} is lower than the binding energy of the least bound nucleon in the $(A - 2, Z)$ nucleus: $E_{\text{exc}} < S_N(A - 2, Z)$, where $S_N(A - 2, Z) =$

$\min\{S_n(A - 2, Z), S_p(A - 2, Z)\}$.² Under this condition, we receive the restriction on the values of the neutrons binding energies: $E_{n1}^b(A, Z) + E_{n2}^b(A, Z) < 2S_n(A, Z) + S_N(A - 2, Z)$.

Values of the separation energies S_n and S_p were taken from [20]. Single-particle energies $E_n^b(A, Z)$ for neutrons in the ${}^{39}_{19}\text{K}$ nucleus were calculated with the WSBETA code [21] using the Blomqvist–Wahlborn parametrization of the Woods–Saxon potential [22]. The calculated value of the neutron separation energy $S_n^{\text{calc}} = 13.08$ MeV is in good agreement with the experimental value $S_n^{\text{exp}} = 13.07$ MeV [20]. We conservatively suppose that contributions to the effective number of objects, $N_{\text{obj}}^{\text{eff}}$, give only paired neutrons (i.e., neutrons with equal values of all quantum numbers, except for the magnetic quantum number) and neglect contributions from other neutrons. Taking into account that the binding energies of such particles are equal, the appropriate equation is as follows: $2E_n^b(A, Z) < 2S_n(A, Z) + S_N(A - 2, Z)$. This condition gives only two nn pairs whose disappearance from ${}^{39}_{19}\text{K}$ will produce relatively low-excited daughter ${}^{37}_{19}\text{K}$, which emit only γ quanta (hence, cannot be transformed to a nucleus with $A < 37$ as a result of ejection of additional nucleons). Substituting the values $N_{\text{nuc1}} = 9.7 \times 10^{27}$, $N_{\text{obj}}^{\text{eff}} = 2$, and $\lim S/t = 1.28$ atom/day in Eq. (1), one gets

$$\lim \tau_{nn} = 4.2 \times 10^{25} \text{ yr at 90\% C.L.}$$

In conclusion, reanalysis of the data of the radiochemical experiment of Fireman [14] allows us to establish the limits $\tau_{nn} > 4.2 \times 10^{25}$ yr and $\tau_{np} > 2.1 \times 10^{25}$ yr at 90% C.L. The τ_{nn} value is near the same as that given recently by the BOREXINO Collaboration ($\tau_{nn} > 4.9 \times 10^{25}$ yr [12]), while the obtained value for τ_{np} is two orders of magnitude higher than that set in [13] and is the most restrictive up-to-date limit for np decays into invisible channels.

REFERENCES

1. P. Langacker, Phys. Rep. **71**, 185 (1981).
2. K. Hagiwara *et al.* (Particle Data Group), Phys. Rev. D **66**, 010001 (2002).
3. F. J. Yndurain, Phys. Lett. B **256**, 15 (1991).
4. N. Arkani-Hamed, S. Dimopoulos, and G. Dvali, Phys. Lett. B **429**, 263 (1998).

¹ Unfortunately, the disappearance of the pp pair results in the creation of stable nucleus ${}^{37}_{17}\text{Cl}$ and, thus, cannot be investigated in this approach.

² Higher excitations of the daughter nucleus will result in the deexcitation process with the emission of mostly n, p , etc., instead of γ quanta, and give not the $(A - 2, Z)$ nucleus but isotopes with lower A and Z values.

5. V. A. Rubakov, Usp. Fiz. Nauk **171**, 913 (2001) [Phys. Usp. **44**, 871 (2001)].
6. J. Hewett and J. March-Russell, in [2].
7. S. N. Gninenko, N. V. Krasnikov, and A. Rubbia, Phys. Rev. D **67**, 075012 (2003).
8. Yu. Kamyshev and E. Kolbe, Phys. Rev. D **67**, 076007 (2003).
9. R. N. Boyd, T. Rauscher, S. D. Reitzner, and P. Vogel, Phys. Rev. D **68**, 074014 (2003).
10. Yu. G. Zdesenko and V. I. Tretyak, Phys. Lett. B **553**, 135 (2003).
11. S. N. Ahmed *et al.*, hep-ex/0310030.
12. H. O. Back *et al.*, Phys. Lett. B **563**, 23 (2003).
13. R. Bernabei *et al.*, Preprint LNGS/EXP-08/03 (2003); *Talk on 4th International Conference on Physics Beyond the Standard Model: Beyond the Desert'03, Castle Ringberg, Tegernsee, Germany* (2003).
14. E. L. Fireman, in *Proceedings of International Conference on Neutrino Physics and Neutrino Astrophysics (Neutrino'77), Baksan Valley, USSR, 1977* (Nauka, Moscow, 1978), Vol. 1, p. 53.
15. R. I. Steinberg and J. C. Evans, in *Proceedings of International Conference on Neutrino Physics and Neutrino Astrophysics (Neutrino'77), Baksan Valley, USSR, 1977* (Nauka, Moscow, 1978), Vol. 2, p. 321.
16. G. J. Feldman and R. D. Cousins, Phys. Rev. D **57**, 3873 (1998).
17. *Table of Isotopes*, Ed. by R. B. Firestone, V. S. Shirley, C. M. Baglin, *et al.*, 8th ed. (Wiley, New York, 1996).
18. J. C. Evans, Jr. and R. I. Steinberg, Science **197**, 989 (1977).
19. R. Bernabei *et al.*, Phys. Lett. B **493**, 12 (2000).
20. G. Audi and A. H. Wapstra, Nucl. Phys. A **595**, 409 (1995).
21. S. Cwiok *et al.*, Comput. Phys. Commun. **46**, 379 (1987).
22. J. Blomqvist and S. Wahlborn, Ark. Fys. **16**, 545 (1960).

Coherent Multiple Scattering Effects and Monte Carlo Method

V. L. Kuzmin^{1,*} and I. V. Meglinski^{2,3}

¹ St. Petersburg Institute of Commerce and Economics, ul. Novorossiiskaya 50, St. Petersburg, 194021 Russia

² Cranfield University, School of Engineering, Cranfield, MK43 0AL, United Kingdom

* e-mail: vladimir.kuzmin@paloma.spbu.ru

³ Saratov State University, ul. Astrakhanskaya 83, Saratov, 410026 Russia

Received December 1, 2003; in final form, January 8, 2004

Based on the comparison of the iteration procedure of solving the Bethe–Salpeter equation and the Monte Carlo method, we developed a method for simulating coherent multiple-scattering effects within the framework of a unified stochastic approach. The time correlation function and the interference component were calculated for the coherent backscattering from a multiply scattering medium. © 2004 MAIK “Nauka/Interperiodica”.

PACS numbers: 42.25.Fx; 11.10.St; 02.70.Uu

Numerical simulation based on the stochastic Monte Carlo method is widely used to calculate the intensity of scattered radiation in randomly inhomogeneous turbid media [1]. However, a special approach is required to apply the method for simulating coherent effects, which manifest themselves even in the presence of strong multiple scattering and have attracted increasing interest in recent years [2–8].

In this work, the stochastic Monte Carlo method is compared with a theoretical approach based on the representation of the Bethe–Salpeter equation in the form of a multiple scattering series to show how this method is generalized within the framework of a unified stochastic approach for calculating time correlations of intensity, coherent backscattering, and other coherent effects.

The field correlation function in an inhomogeneous dispersive medium with random space–time fluctuations of the dielectric constant is described by the integral Bethe–Salpeter equation

$$\Gamma(\mathbf{R}_2, \mathbf{R}_1, t | \mathbf{k}_s, \mathbf{k}_i) = \mu p_t(\mathbf{k}_i - \mathbf{k}_s) \delta(\mathbf{R}_2 - \mathbf{R}_1) + \mu \int p_t(\mathbf{k}_{23} - \mathbf{k}_s) \Lambda(R_{23}) \Gamma(R_3, \mathbf{R}_1, t | \mathbf{k}_{31}, \mathbf{k}_i) d\mathbf{R}_3. \quad (1)$$

Here, the Green’s function (propagator) $\Gamma(\mathbf{R}_2, \mathbf{R}_1, t | \mathbf{k}_s, \mathbf{k}_i)$ of the Bethe–Salpeter equation describes the propagation of a pair of time-shifted (by t) complex conjugate fields from the point \mathbf{R}_1 with the incident wave vector \mathbf{k}_i to the point \mathbf{R}_2 with the outgoing wave vector \mathbf{k}_s ; $k_s = k_i = k = nk_0$, where $k_0 = 2\pi/\lambda$ is the wavenumber, λ is the wavelength; $n = n_1 + in_2$ is the refractive index of a medium; and $(2n_2k_0)^{-1} = l$ is the photon mean free path. For simplicity, we restrict ourselves only to the case where the intrinsic absorption is absent and light losses are caused only by elastic scattering. In this case,

the scattering coefficient is $\mu = l^{-1}$. The function $\Lambda(R) = R^{-2} \exp(-R/l)$ is the product of a complex conjugate pair of Green’s functions of the corresponding wave equation and describes the radiation propagation between two scattering events. The function $p_t(\mathbf{k}_i - \mathbf{k}_s)$ is expressed in terms of the Fourier transform of the pair correlation function of dielectric constant fluctuations and coincides at $t = 0$ with the scattering phase function $p_0(\mathbf{k}_i - \mathbf{k}_s) = p(\mathbf{k}_i - \mathbf{k}_s)$.

Let a scattering medium occupy the half-space $z > 0$, where z is the Cartesian coordinate normal to the medium boundary. For the normal incidence and backscattering, the incoherent component of the time correlation function is described by the ladder-diagram series and has the form

$$C^{(L)}(t | \mathbf{k}_s, \mathbf{k}_i) = \int d\mathbf{R}_1 d\mathbf{R}_2 \times \Gamma(\mathbf{R}_2, \mathbf{R}_1, t | \mathbf{k}_s, \mathbf{k}_i) \exp[-\mu(z_1 + z_2)]. \quad (2)$$

For scattering angles θ_s close to 180° , the interference component caused by the cyclic [9, 10] or fan diagrams is comparable with the ladder component:

$$C^{(V)}(t | \mathbf{k}_s, \mathbf{k}_i) = \int d\mathbf{R}_1 d\mathbf{R}_2 \times \left[\Gamma\left(\mathbf{R}_2, \mathbf{R}_1, t \left| \frac{\mathbf{k}_s - \mathbf{k}_i}{2}, \frac{\mathbf{k}_i - \mathbf{k}_s}{2} \right. \right) - \mu p_t(\mathbf{k}_i - \mathbf{k}_s) \delta(\mathbf{R}_2 - \mathbf{R}_1) \right] \times \exp[-\mu(z_1 + z_2) + ik_0(x_1 - x_2) \sin \theta_s]. \quad (3)$$

The incident and scattered beams lie in the (x, z) plane.

Intensity of backscattered light as a function of the layer thickness L for various anisotropy parameters

$\overline{\cos\theta}$	$L = l^*$	$L = 2l^*$	$L = 5l^*$	$L = 10l^*$	∞
0	0.3481	0.5254	0.7507	0.8665	1
0.9	0.3214	0.5318	0.7784	0.9003	1

At $t = 0$, Eq. (2) describes the backscattering intensity. Correspondingly, Eq. (3) determines the peak in the coherent backscattering.

By integrating the Bethe–Salpeter equation, one arrives at a series that is usually illustrated by a series of ladder diagrams.

Let us compare the analytic procedure of summing ladder-diagram series with the Monte Carlo method. The first term of the iterative series describes single scattering, the second term describes two scattering events, etc. Similarly, the Monte Carlo method describes the radiation propagation as a stochastic process consisting of 1, 2, ..., N scattering events. The addition of one ladder section $\Lambda(R_{nn+1})p_0(\mathbf{k}_{nn+1} - \mathbf{k}_{n+1})$ in the theoretical description is realized in the numerical experiment by modeling the photon paths through a certain distance s to the next scattering event. The main assumption in the stochastic Monte Carlo method consists of postulating the distribution law $f(s) = \mu \exp(-\mu s)$ for the photon mean free path as a random variable s [11]. It follows from this distribution that $s = -\mu^{-1} \ln \xi$, where ξ is the probability that the mean free path is no less than s . In the Monte Carlo method, the arbitrary ξ value is chosen in the $[0, 1]$ interval using a random number generator. The change in the direction of motion of the photon package in each elastic scattering event is determined by the scattering phase function.

Physically, the series arising upon the iteration of Eq. (1) is a series in scattering multiplicity. If the integration with respect to R_i is replaced by a random choice $R_i = s$ and the integration with respect to \mathbf{R}_i is realized by a random choice of angles with the statistical weight determined by the phase function, then the solution of the Bethe–Salpeter equation is simulated by the Monte Carlo scheme described above, making it possible to use it for calculating coherent effects.

The majority of applications [12, 13] are devoted to the diffusion mechanism of inhomogeneity time evolution, for which the time correlation function of intensity fluctuations can be represented as the product of static correlation function and exponential

$$p_t(q) \approx p_0(q) \exp(-D_s q^2 t), \quad (4)$$

where D_s is the self-diffusion coefficient. The only difference between the calculation of the time correlation function and the calculation of intensity is that the

weight of the photon package is multiplied by the phase function $p_t(\mathbf{k}_n - \mathbf{k}_{n-1})$ in each scattering event.

The number of incident photons varied in the range 10^5 – 10^7 . The simulation of photon trajectory was terminated when the number of scattering events exceeded 10^4 . We also disregarded photons whose statistical weights became less than 10^{-3} . This neglect leads to an error no higher than 10^{-5} , because, according to our estimates, the probability of detecting such a photon on the surface is no higher than 10^{-2} . The accuracy of calculated parameters was tested by the stability of numerical values upon increasing the sample size. For a number of 10^5 , the intensity is stable with an accuracy of no less than four decimal places.

The time correlation function of the field $g_1(t)$ was calculated for media with various anisotropy factors $\overline{\cos\theta} = 0, 0.5, \text{ and } 0.9$. The Henyey–Greenstein phase function was used in simulation. In terms of $\sqrt{t/\tau}$, where $\tau = 1/D_s k^2$ is the characteristic diffusion time of a scattering particle through a distance on the order of the wavelength, the time correlation function is virtually universal and is independent of the anisotropy of single scattering, in agreement with experiments [12, 13] and theoretical solution in the P_1 approximation [14], while the specificity of the scattering system is taken into account upon the transition to the description in units of characteristic time τ . The dependence obtained for the time correlation function is well described by the formula $g_1(t) \propto \exp(-\gamma \sqrt{6t/\tau})$ proposed in [13].

The time correlation function was calculated for layers of different thickness. The corresponding dependence on the average cosine $\overline{\cos\theta}$ of the single-scattering angle is weak enough for finite-thickness layers, as is seen in the table, where $l^* = l(1 - \overline{\cos\theta})^{-1}$ is the transport mean free path.

Figure 1 shows the results of simulation of the field time correlation functions for finite-thickness layers with $\overline{\cos\theta} = 0.9$. As is seen, the diffusion character of light propagation with a linear dependence on $\sqrt{t/\tau}$ reveals itself at increasingly large times with a decrease in thickness. Good agreement with the experimental data is noteworthy: Fig. 1 almost exactly reproduces Fig. 2 from [13].

Figure 2 also shows the angular dependence of the coherent backscattering peak calculated for $\overline{\cos\theta} = 0, 0.5, \text{ and } 0.9$. It follows from Eq. (3) that, in the case of normal incidence and small backscattering angles, the difference from the expression for the intensity of the incoherent component consists only in the presence of the additional factor $\exp(i\mathbf{q}_\perp(\boldsymbol{\rho}_1 - \boldsymbol{\rho}_2))$, which can be replaced by $\cos(\mathbf{q}_\perp(\boldsymbol{\rho}_1 - \boldsymbol{\rho}_2))$ because of the translational invariance about the transverse coordinates $\boldsymbol{\rho}$.

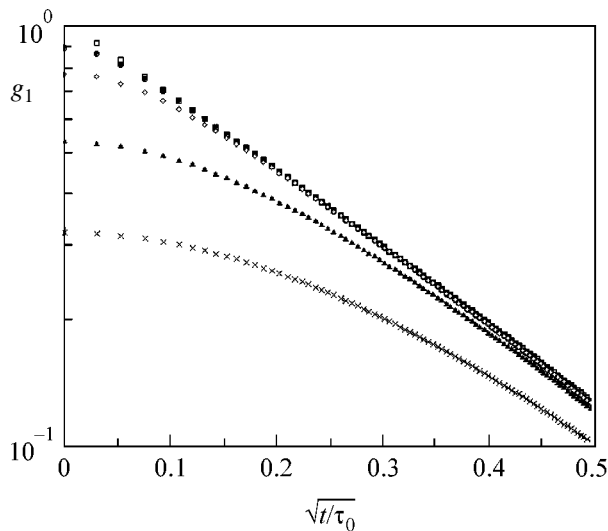


Fig. 1. Time correlation functions g_1 of backscattered radiation for layers with thickness $L = (\times) l^*$, $(\blacktriangle) 2l^*$, $(\diamond) 5l^*$, $(\bullet) 10l^*$, and $(\square) \infty$ (semi-infinite medium). All data are normalized to the intensity of light diffusively reflected from the semi-infinite medium. The optical parameters of the medium are $\mu = 30 \text{ mm}^{-1}$ and $\overline{\cos\theta} = 0.9$.

Then, when calculating the intensity of the backscattering coherent component, one should, first, multiply the total weight of photon packages arriving with vector \mathbf{k}_s at distance ρ from the entry point at the interface by the factor $\cos(\mathbf{q}_\perp \cdot \boldsymbol{\rho})$ and, second, take the sum over the entire surface.

Similarly to the time correlations, the angular dependence of the coherent backscattering peak intensity proves to be universal in the dimensionless variable $\tilde{q} = kl^* \sin\theta_s$ and is well described by the formula $I_{\text{CBS}} \propto \exp(-\gamma kl^* \sin\theta_s)$ with $\gamma = 2$. Note that the obtained universal dependence $I_{\text{CBS}} \propto \exp(-\gamma kl^* \sin\theta_s)$ with $\gamma = 2$ differs significantly from the dependence [15]

$$I_{\text{CBS}}^{\text{diff}} \propto 1 - 2 \frac{(1 + z^*)^2}{1 + 2z^*} kl^* \sin\theta_s,$$

predicted in the diffusion approximation for $kl^* \sin\theta_s \ll 1$, where $z^* = 0.71(1 - \overline{\cos\theta})^{-1}$. This formula gives the slope $\gamma^{(\text{diff})} = 2.3$ for $\overline{\cos\theta} = 0$ and $\gamma^{(\text{diff})} = 0.71$ for $\overline{\cos\theta} \rightarrow 1$.

Contrary to the diffusion approximation, which predicts that the linear slope of the coherent backscattering peak decreases with an increase in anisotropy, the dependence calculated by us indicates the universal character of a decrease. If the phase function is strongly anisotropic, the coherence effects can be quite pronounced, despite the smallness of these parameters. In particular, the decay of intensity time correlations is governed by the parameter t/τ , which can be much

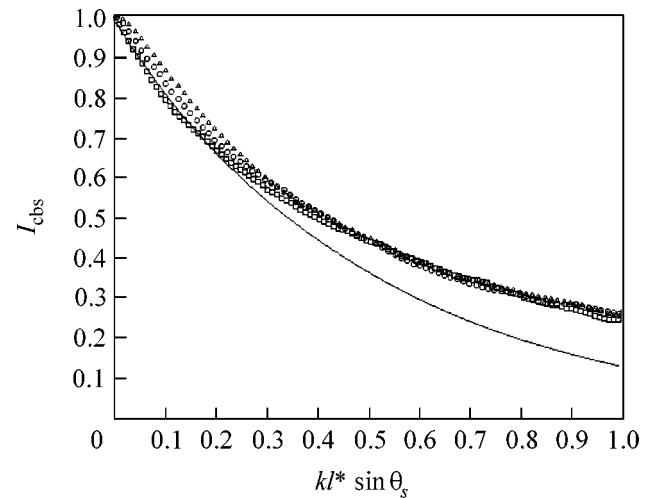


Fig. 2. Peak intensity of coherent backscattering vs. the dimensionless parameter $kl^* \sin\theta_s$; $\lambda = 0.6 \mu\text{m}$; $n_1 = 1$; $\mu = 30 \text{ mm}^{-1}$; $\overline{\cos\theta} = (\square) 0$, $(\circ) 0.5$, and $(\blacktriangle) 0.9$; and the solid line is the $\exp(-2kl^* \sin\theta_s)$ approximation.

greater than the parameter $(t/\tau)(l/l^*)$. It is precisely due to this fact that the intensity correlation functions are described by the multiple-scattering theory even if they decrease by two orders of magnitude.

In this work, the coherent effects in multiple scattering have been simulated within the framework of a unified stochastic approach. Similar calculations can easily be carried out for suspensions that are usually treated as a system of hard spheres [16]. The phase function for this system is represented as the product of the Mie form factor and the Percus–Yevick structure factor.

The comparative analysis carried out in this work enables one to considerably simplify the simulation of radiation transport and coherent effects in randomly inhomogeneous strongly scattering media, such as liquid crystals, tissues, etc., and to extend the application field of these methods.

We are grateful to D.Yu. Churmakov for assistance in calculations and V.P. Romanov for valuable advice. This work was supported by the Russian Foundation for Basic Research (project no. 02-02-16577), the Royal Society (grant no. 15298), and NATO (grant no. PST.CLG.979652).

REFERENCES

1. V. P. Kandidov, Usp. Fiz. Nauk **166**, 1309 (1996) [Phys. Usp. **39**, 1243 (1996)].
2. M. Ospeck and S. Fraden, Phys. Rev. E **49**, 4578 (1994).
3. T. Iwai, H. Furukawa, and T. Asakura, Opt. Rev. **2**, 413 (1995).
4. K. Ishii, T. Iwai, and T. Asakura, Opt. Rev. **4**, 643 (1997).

5. S. E. Skipetrov and S. S. Chesnokov, *Kvantovaya Élektron.* (Moscow) **25**, 753 (1998).
6. R. Lenke and G. Maret, *Eur. Phys. J. B* **17**, 171 (2000).
7. S. E. Skipetrov and I. V. Meglinskiĭ, *Zh. Éksp. Teor. Fiz.* **113**, 1213 (1998) [*JETP* **86**, 661 (1998)].
8. R. Lenke, R. Tweer, and G. Maret, *J. Opt. A: Pure Appl. Opt.* **4**, 293 (2002).
9. Yu. N. Barabanenkov, *Izv. Vyssh. Uchebn. Zaved., Radiofiz.* **16**, 88 (1973).
10. A. A. Golubentsev, *Zh. Éksp. Teor. Fiz.* **86**, 47 (1984) [*Sov. Phys. JETP* **59**, 26 (1984)].
11. I. M. Sobol', *The Monte Carlo Method* (Nauka, Moscow, 1985).
12. G. Maret and P. Z. Wolf, *Z. Phys. B* **65**, 409 (1987).
13. D. J. Pine, D. A. Weitz, P. M. Chaikin, and E. Herbolzheimer, *Phys. Rev. Lett.* **60**, 1134 (1988).
14. V. L. Kuzmin, V. P. Romanov, and E. V. Aksenova, *Phys. Rev. E* **65**, 016601 (2002).
15. E. Akkermans, P. E. Wolf, R. Maynard, *et al.*, *J. Phys. (Paris)* **49**, 77 (1988).
16. V. L. Kuz'min, V. P. Romanov, and I. V. Meglinskiĭ, *Opt. Spektrosk.* **96**, 139 (2004) [*Opt. Spectrosc.* **96**, 106 (2004)].

Translated by R. Tyapaev

On the Two-Parametric Theory of Superconductivity

R. O. Zaitsev

Russian Research Centre Kurchatov Institute, pl. Kurchatova 1, Moscow, 123182 Russia

Received December 1, 2003

The concept of spin fluctuations in the Hubbard model is used for deriving a closed system of equations for the superconducting order parameter Δ and spin susceptibility. The limiting cases of low temperatures and temperatures close to the superconducting transition temperature are considered. The temperature dependences of the parameter Δ and the Knight shift are obtained. The conditions under which the second-order phase transition turns to the first-order phase transition are established. © 2004 MAIK "Nauka/Interperiodica".

PACS numbers: 74.20.De; 71.10.Fd; 71.27.+a

In studies of the possibility of superconductivity in the Hubbard model [1], it was found that the effect of spin fluctuations reduces to the appearance of a finite spin-flip relaxation rate ($1/\tau_s$) proportional to the mean-square spin fluctuation K_s : $1/\tau_s \sim K_s$. In turn, the quantity K_s is proportional to the product $K_s \sim T\chi_s$ of the temperature and spin susceptibility. In the metallic nonsuperconducting phase, the susceptibility is virtually independent of temperature, so that the reciprocal relaxation time proves to be directly proportional to temperature.

In the Hubbard model, one has

$$\frac{1}{\tau_{sn}} = 12\pi v_n \mu^2 T \chi_n, \quad (1)$$

where v_n is the density of states at the Fermi surface and μ is the Fermi energy.

In the Emery–Hirsch model,

$$\frac{1}{\tau_{sn}} = 3\pi v_n \frac{(\epsilon_p \epsilon_d)^2}{2\mu^2} T (\chi_p + \chi_d), \quad (2)$$

where $\epsilon_{p,d}$ are the energies of the one-particle p and d states and $\chi_{p,d}$ are the susceptibilities of the p and d sub-systems.

In the superconducting state, the spin susceptibility becomes temperature-dependent because of a decrease in the number of normal electrons. The spin susceptibility normalized to the susceptibility of the normal phase, χ_s/χ_n , can be expressed in terms of the reciprocal spin-flip relaxation time using the well-known relation [2, 3]

$$\frac{\chi_s}{\chi_n} = 1 - \left(\frac{\Delta}{2\pi T}\right)^2 \sum_{k>0}^{\infty} \left\{ \left[\left(\frac{\Delta}{2\pi T}\right)^2 + u_k^2 \right]^{3/2} - \left[\left(\frac{\Delta}{2\pi T}\right)^2 + 2u_k^2 \right] \frac{\zeta(T)}{3} \right\}^{-1}. \quad (3)$$

The quantity u_k in this equation can be expressed as a function of the half-integer parameter $k + 1/2$:

$$w_k = k + \frac{1}{2} = u_k \left\{ 1 - \frac{\zeta(T)}{\sqrt{u_k^2 + (\Delta/2\pi T)^2}} \right\}, \quad (4)$$

$$\zeta(T) = \frac{1}{2\pi T \tau_s}.$$

The equation for the superconducting order parameter Δ can be written as the sum

$$\ln \frac{T}{T_{c0}} = \sum_{k>0} \left\{ \frac{1}{\sqrt{u_k^2 + (\Delta/2\pi T)^2}} - \frac{1}{k + 1/2} \right\}, \quad (5)$$

where T_{c0} is the superconducting transition temperature calculated in the limit $\tau_s \rightarrow \infty$.

The system of Eqs. (3)–(5) assumes a closed form if we write the relation between the relaxation time and the spin susceptibility as

$$\zeta(T) = \frac{1}{2\pi T \tau_s} = \frac{1}{2\pi T \tau_{sn}} \frac{\tau_{sn}}{\tau_s} = \frac{1}{2\pi T \tau_{sn} \chi_n} \chi_s = \zeta_n \frac{\chi_s}{\chi_n}. \quad (6)$$

As was noted above, the quantity $1/\tau_{sn}$ is directly proportional to temperature, so that parameter ζ_n is a constant quantity dependent only on the properties of the normal metal but independent of temperature. Below, we assume that it does not exceed unity.

Equations (3)–(6) form a closed system of equations for determining the superconducting order parameter Δ and the depairing parameter

$$\phi_s = 1/\Delta \tau_s = 2\pi T \zeta(T)/\Delta.$$

To clarify the general picture, we note that the main Eq. (4) has the form of the fourth-degree equation in

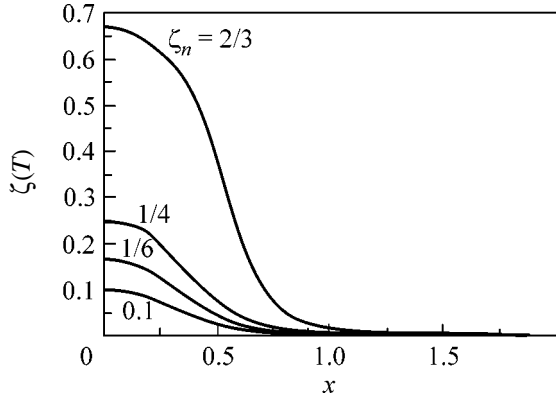


Fig. 1. Dependence of the depairing parameter $\zeta(T)$ on $\Delta/2\pi T$.

variable u_k , so that we can obtain the explicit dependence of u_k on the discrete variable $w_k = k + 1/2$:

$$u_k^4 - 2w_k u_k^3 + (x^2 + w_k^2 - \zeta^2)u_k^2 - 2x^2 w_k u_k + x^2 w_k^2 = 0. \quad (7)$$

In accordance with the general theory of algebraic equations, the solution to Eq. (7) can be expressed through one of the real roots of the following cubic equation:

$$z^3 - (w_k^2 + x^2 - \zeta^2)z^2 - 4x^2 \zeta^2 w_k^2 = 0, \quad (8)$$

$$x = \Delta/2\pi T, \quad \zeta \equiv \xi(T).$$

In our case with $\zeta < \zeta_n < 1$, we have only a single real root

$$z = \frac{s^{1/3}}{6} + \frac{2a^2}{3s^{1/3}} + \frac{a}{3}, \quad x = \frac{\Delta}{2\pi T},$$

$$a = w_k^2 - \zeta^2 + x^2, \quad b = 4x^2 w_k^2 \zeta^2, \quad (9)$$

$$s = 4(2a^3 + 27b) + 12\sqrt{3b(4a^3 + 27b)}.$$

In this case, the required function u_k is defined through z after solving one of the two quadratic equations (for details, see, for example, [4]).

This gives

$$u_k = \frac{w_k}{2} + \frac{1}{2}\sqrt{z - x^2 + \zeta^2} + \frac{1}{2} \times \sqrt{w_k^2 + 2w_k\sqrt{z - x^2 + \zeta^2} - z - x^2 + \zeta^2 - 2w_k \frac{(z - 2x^2)}{\sqrt{z - x^2 + \zeta^2}}}. \quad (10)$$

For each given value ζ_n , self-consistency condition (6) assumes the form of dependence $\zeta = f(x)$. In the new

variables, we obtain the following equation:

$$\frac{\zeta(T)}{\zeta_n} = \frac{\chi_s}{\chi_n}, \text{ or}$$

$$\frac{\zeta}{\zeta_n} = 1 - x^2 \sum_{k>0}^{\infty} \left\{ [x^2 + u_k^2]^{3/2} - [x^2 + 2u_k^2] \frac{\zeta}{3} \right\}^{-1}. \quad (11)$$

The numerical solution of this equation is presented in Fig. 1 for four different values of ζ_n .

Thus, for all $\zeta_n < 1$, the quantity $\Delta/2\pi T$ is in one-to-one correspondence with the parameter $\zeta(T)$. However, the temperature dependence of these parameters is not always unambiguous.

In the low-temperature range $T \ll \Delta$ the susceptibility is proportional to the density of normal electrons and can be determined from relations (3) and (4) in the limit $\zeta(T) = 0$ and $u_k = k + 1/2 = w_k$:

$$\zeta(T) \approx \zeta_n \frac{\chi_s}{\chi_n} = \zeta_n \sqrt{\frac{2\pi\Delta_0}{T}} \exp\left(-\frac{\Delta_0}{T}\right). \quad (12)$$

When written in this form, it coincides with the well-known Yosida formula [5].

In this limit, one can perform summation in Eq. (5) for Δ :

$$\ln \frac{\Delta\gamma}{\pi T_{c0}} = \ln \frac{\Delta}{\Delta_0} = 2 \sum_{k=1}^{\infty} (-1)^k K_0\left(\frac{k\Delta}{T}\right). \quad (13)$$

Here, the natural notation $\Delta_0 = \Delta(0) = \pi T_{c0}/\gamma$ is introduced, where $\gamma = \exp(C)$ and $C \approx 0.577$ is the Euler constant.

The next approximation is found by the expansion in parameter $\zeta(T)$:

$$u_k \approx w_k + \zeta(T) \frac{w_k}{\sqrt{w_k^2 + (\Delta/2\pi T)^2}}. \quad (14)$$

It turns out that, in addition to the regular quasiparticle term, the low-temperature correction to Δ_0 also contains the contribution from paramagnetic fluctuations:

$$\ln \frac{\Delta}{\Delta_0} \approx -\sqrt{\frac{2\pi T}{\Delta_0}} \exp\left(-\frac{\Delta_0}{T}\right) - \frac{\pi}{4} \zeta_n \frac{\chi_s}{\chi_n} \frac{2\pi T}{\Delta_0}. \quad (15)$$

Using expansion (14), we obtain

$$\Delta \approx \Delta_0 \left\{ 1 - \left[1 + \zeta_n \frac{\pi}{4} \right] \sqrt{\frac{2\pi T}{\Delta_0}} \exp\left(-\frac{\Delta_0}{T}\right) \right\}. \quad (16)$$

The contribution to the magnetic susceptibility from the paramagnetic fluctuations turns out to be small compared to (12),

$$\frac{\chi_s}{\chi_n} \approx \sqrt{\frac{2\pi\Delta_0}{T}} \exp\left(-\frac{\Delta_0}{T}\right) + \frac{\pi}{12} \zeta_n \sqrt{\frac{2\pi T}{\Delta_0}} \exp\left(-\frac{\Delta_0}{T}\right). \quad (17)$$

Next, we consider equations linearized with respect to Δ .

The equation for the transition temperature can be found from Eqs. (5) and (6) with $\chi_s = \chi_n$ and $\Delta = 0$:

$$\ln \frac{T_c}{T_{c0}} = \sum_{k>0}^{\infty} \left\{ \frac{1}{k+1/2+\zeta_n} - \frac{1}{(k+1/2)} \right\}. \quad (18)$$

After the summation, we find

$$\frac{T_c}{T_{c0}} = \exp(\psi(1/2) - \psi(\zeta_n + 1/2)). \quad (19)$$

In the limit $T = 0$, $\chi_s = 0$ and we have $u_k = k + 1/2$. Then, using Eq. (5), we arrive at the classical relation

$$\frac{2\Delta_0(0)}{T_{c0}} = \frac{2\pi}{\gamma} \approx 3.527. \quad (20)$$

From the comparison of Eqs. (13) and (19), we find the ratio $2\Delta(0)/T_c$,

$$\frac{2\Delta(0)}{T_c} = 8\pi \exp\left[\psi\left(\frac{1}{2} + \zeta_n\right)\right], \quad (21)$$

which proves to be greater than its classical value $2\pi/\gamma \approx 3.53\dots$. The corresponding curve is shown in Fig. 2.

In the superconducting region $T \leq T_c$, a decrease in the spin susceptibility χ_s can be expressed in terms of the temperature slope of parameter $\Delta(T)$.

By expanding the self-consistency equations in small parameter $(\Delta/2\pi T)^2$, we obtain

$$-\ln\left(\frac{T}{T_{c0}}\right) - \psi\left(\frac{1}{2} + \zeta(T)\right) + \psi\left(\frac{1}{2}\right) = B_1(\zeta_n) \left(\frac{\Delta}{2\pi T}\right)^2, \quad (22)$$

where

$$B_1(\zeta_n) = -\frac{1}{4}\psi^{(2)}\left(\zeta_n + \frac{1}{2}\right) - \frac{\zeta_n}{12}\psi^{(3)}\left(\zeta_n + \frac{1}{2}\right).$$

Here, $\psi^{(k)}(x)$ are the k th derivatives of $\psi(x)$, while the obtained equation coincides with the well-known relations for superconductors with paramagnetic impurities [6].

In order to determine the temperature slope with which Δ turns to zero, it suffices to expand the left-hand side of Eq. (22) in powers of $(T_c - T)/T_c$ and $\zeta(T) - \zeta_n$. This gives

$$\frac{T_c - T}{T_c} - \psi^{(1)}\left(\frac{1}{2} + \zeta_n\right)(\zeta(T) - \zeta_n) = B_1(\zeta_n) \left(\frac{\Delta}{2\pi T}\right)^2. \quad (23)$$

Here, the superconducting transition temperature and the correction to the depairing parameter are deter-

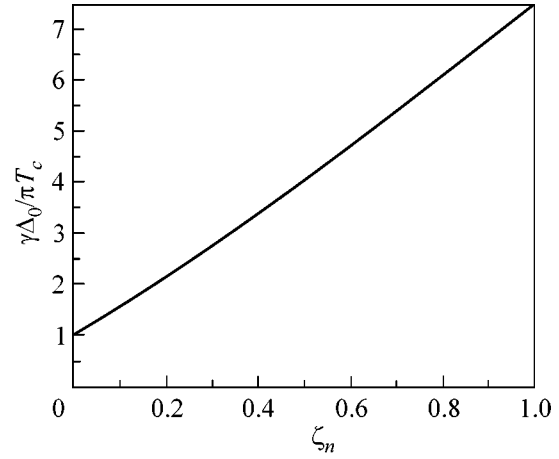


Fig. 2. Dependence of $2\Delta_0/T_c$ on the depairing parameter ζ_n .

mined from the conditions

$$\begin{aligned} -\ln\left(\frac{T_c}{T_{c0}}\right) &= \psi\left(\frac{1}{2} + \zeta_n\right) - \psi\left(\frac{1}{2}\right); \\ \frac{\zeta(T) - \zeta_n}{\zeta_n} &= \frac{\chi_s - \chi_n}{\chi_n}. \end{aligned} \quad (24)$$

The first nonvanishing correction to the susceptibility can be found by expanding Eqs. (3) and (4) in powers of $\Delta/2\pi T$:

$$\begin{aligned} \frac{\chi_s}{\chi_n} &= 1 - \left(\frac{\Delta}{2\pi T}\right)^2 \frac{3}{2\zeta_n^2} \\ &\times \left\{ \frac{3}{2} \left[\psi\left(\zeta_n + \frac{1}{2}\right) - \psi\left(\frac{\zeta_n}{3} + \frac{1}{2}\right) \right] - \zeta_n \psi^{(1)}\left(\zeta_n + \frac{1}{2}\right) \right\}. \end{aligned} \quad (25)$$

This gives for the temperature slope

$$\left(\frac{\Delta}{2\pi T_c}\right)^2 = \frac{T_c - T}{T_c} \frac{1}{(B_1(\zeta_n) - B_2(\zeta_n))}, \quad (26)$$

where

$$\begin{aligned} B_1(\zeta_n) &= -\frac{1}{4}\psi^{(2)}\left(\zeta_n + \frac{1}{2}\right) - \frac{\zeta_n}{12}\psi^{(3)}\left(\zeta_n + \frac{1}{2}\right), \\ B_2(\zeta_n) &= \frac{3}{2\zeta_n}\psi^{(1)}\left(\zeta_n + \frac{1}{2}\right) \end{aligned} \quad (27)$$

$$\times \left\{ \frac{3}{2} \left[\psi\left(\zeta_n + \frac{1}{2}\right) - \psi\left(\frac{\zeta_n}{3} + \frac{1}{2}\right) \right] - \zeta_n \psi^{(1)}\left(\zeta_n + \frac{1}{2}\right) \right\}.$$

It can be seen that, when the temperature decreases below $T \leq T_c$, a decrease in the spin susceptibility χ_s is accompanied by an increase (in absolute value) in the temperature slope of parameter $\Delta(T)$ because of the

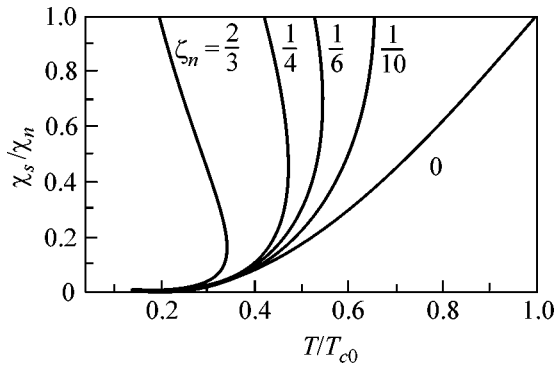


Fig. 3. Temperature dependence of the spin susceptibility $\chi_s(T)/\chi_n$ for various values of parameter ζ_n .

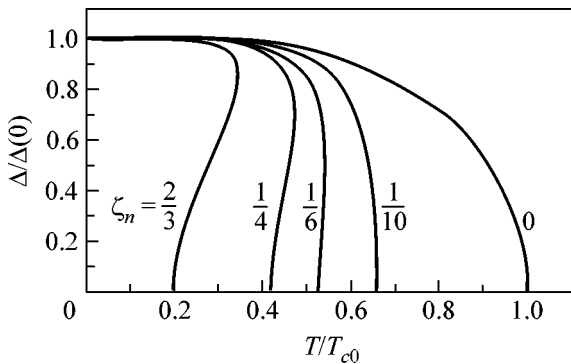


Fig. 4. Temperature dependence of the superconducting order parameter $\Delta(T)/\Delta_0$ for various values of parameter ζ_n .

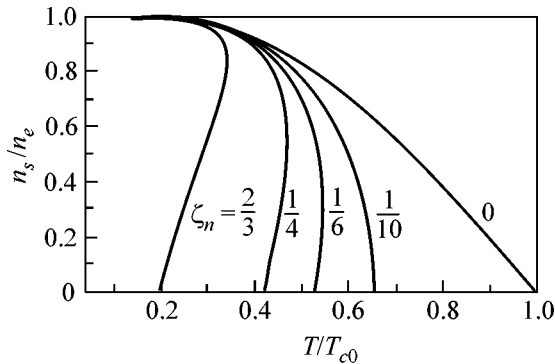


Fig. 5. Temperature dependence of the density $n_s(T)/n_e$ of superconducting electrons for various values of parameter ζ_n .

appearance of the additional coefficient $B_2(\zeta_n)$. For the critical value $\zeta_c \approx 0.105$, the coefficients of Δ^2 vanishes.

In the low-temperature range, where the intensity of spin fluctuations is exponentially small, the physical properties of the superconductor are qualitatively the same as for an ideal superconductor. The energy gap in the excitation spectrum coincides with Δ , the density of states has a root singularity, and the ground-state energy

can be expressed in terms of Δ using the same formula as in the BCS theory. The formulas for the Knight shift and the specific heat in this range have the same exponential form but with different preexponential factors.

As the temperature increases, the spin-flip relaxation rate increases in parallel with the increase in the spin susceptibility. In the vicinity of the transition point, the temperature slope of spin susceptibility is determined by expansion (25). The temperature slope of parameter Δ is determined from formula (26). The susceptibility curves are shown in Fig. 3, from which one can see that the expansion in powers of the distance from the transition point is valid only for extremely small values of parameter $\zeta_n \ll 1$. In the range $\zeta_n \ll 1$, our equations are equivalent to those in the theory of superconductors with a low concentration of paramagnetic impurities [6]. However, even for $\zeta_n \approx 1/10$, a decrease in the spin fluctuations with increasing number of superconducting electrons becomes so rapid that the superconducting order parameter and the density of superconducting electrons $n_s/n_e = 1 - \chi_s/\chi_n$ become increasing functions of temperature (Figs. 4, 5).

Hence, it follows that, starting with the critical value ζ_c , our system becomes unstable, leading to a first-order phase transition. If $\zeta_n > \zeta_c$, the transition temperature determined from Eq. (19) should be treated as a supercooling temperature. In the intermediate range between the supercooling and superheating temperatures, superconductivity exists in a mixed phase whose physical properties deserve special analysis.

Thus, spin fluctuations appreciably reduce the effective BCS constant that determines the superconducting transition temperature, as compared to the constant determining the energy gap in the limit $T \rightarrow 0$. As a result, it has become possible to explain the experimentally observed value of parameter $2\Delta(0)/T_c$ that is higher than in the BCS theory. At the same time, the reverse effect of Cooper pairing on spin fluctuations leads to their suppression. Under certain conditions, this effect causes a rapid increase in parameter Δ with temperature and the occurrence of a first-order phase transition with a small heat release.

REFERENCES

1. R. O. Zaitsev, Pis'ma Zh. Éksp. Teor. Fiz. **56**, 355 (1992) [JETP Lett. **56**, 339 (1992)].
2. A. A. Abrikosov and L. P. Gor'kov, Zh. Éksp. Teor. Fiz. **42**, 1088 (1962) [Sov. Phys. JETP **15**, 752 (1962)].
3. L. P. Gor'kov and A. I. Rusinov, Zh. Éksp. Teor. Fiz. **46**, 1363 (1964) [Sov. Phys. JETP **19**, 922 (1964)].
4. *Handbook of Mathematical Functions*, Ed. by M. Abramowitz and I. A. Stegun, 2nd ed. (Dover, New York, 1972; Nauka, Moscow, 1979).
5. K. Yosida, Phys. Rev. **110**, 769 (1958).
6. A. A. Abrikosov and L. P. Gor'kov, Zh. Éksp. Teor. Fiz. **39**, 1781 (1960) [Sov. Phys. JETP **12**, 1243 (1960)].

Translated by N. Wadhwa

Probing Structural Relaxation in Complex Fluids by Critical Fluctuations[†]

A. F. Kostko^{1,2}, M. A. Anisimov^{1,*}, and J. V. Sengers¹

¹ Institute for Physical Science and Technology, Department of Chemical Engineering, University of Maryland, College Park, MD 20742, USA

² Department of Physics, St. Petersburg State University of Refrigeration and Food Engineering, St. Petersburg, 191002 Russia

*e-mail: anisimov@ipst.umd.edu

Received December 16, 2003

Complex fluids, such as polymer solutions and blends, colloids, and gels, are of growing interest in fundamental and applied soft-condensed-matter science. A common feature of all such systems is the presence of a mesoscopic structural length scale intermediate between the atomic and macroscopic scales. This mesoscopic structure of complex fluids is often fragile and sensitive to external perturbations. Complex fluids are frequently viscoelastic (showing a combination of viscous and elastic behavior), with their dynamic response depending on the time and length scales. Recently, noninvasive methods to infer the rheological response of complex fluids have gained popularity through the technique of microrheology, where the diffusion of probe spheres in a viscoelastic fluid is monitored with the aid of light scattering or microscopy. Here, we propose an alternative to traditional microrheology that does not require doping of probe particles in the fluid (which can sometimes drastically alter the molecular environment). Instead, our proposed method makes use of the phenomenon of “avoided crossing” between modes associated with the structural relaxation and critical fluctuations that are spontaneously generated in the system. © 2004 MAIK “Nauka/Interperiodica”.

PACS numbers: 61.25.Hq; 83.80.Rs; 83.85.Ei

A liquid mixture in the vicinity of a critical point of mixing exhibits large concentration fluctuations. The dynamics of such critical concentration fluctuations in molecular liquids is well understood: the fluctuations decay exponentially with a diffusive relaxation time [1]

$$\tau_q = \frac{1}{D(q, \xi)q^2}, \quad (1)$$

where q is the wave number of the critical fluctuations, ξ is the spatial correlation length of the fluctuations, and D is the mesoscopic (q -dependent) diffusion coefficient. D vanishes at the critical point in the limit of zero wave number approximately as $\xi^{-1} \sim \varepsilon^{0.63}$, where $\varepsilon = (T - T_c)/T$ is the reduced distance between the temperature T and the critical temperature T_c . In molecular fluids, the q -dependent diffusion coefficient is well described by the mode-coupling theory of critical dynamics [2, 3]:

$$D(q, \xi) = \frac{k_B T}{6\pi\xi\eta_{\text{app}}} \frac{K(q, \xi)}{q^2} \left[1 + \left(\frac{q\xi}{2} \right)^2 \right]^{\frac{z_\eta}{2}} \Omega\left(\frac{\xi}{\xi_D}\right), \quad (2)$$

where k_B is Boltzmann's constant and the apparent viscosity η_{app} is expected to be equal to the solution vis-

cosity η measured by macrorheology; $z_\eta \approx 0.065$ [4] is a universal dynamic scaling exponent. The function $K(q, \xi)$ is a universal (Kawasaki) function with $K(q\xi \rightarrow 0) = 1$; the function $\Omega(\xi/\xi_D) = 2/\pi \arctan(\xi/\xi_D)$ is an approximated dynamic crossover function, where ξ_D is a cutoff length for the critical fluctuations [5, 6].

However, new phenomena emerge in a complex fluid where ξ_D is a mesoscopic length that may compete with the correlation length ξ of the concentration fluctuations. The presence of two mesoscale lengths in near-critical complex fluids causes the appearance of two dynamic modes: one will be a diffusive decay of the critical concentration fluctuations and the other one will be a structural relaxation mode, which often reveals itself as viscoelastic relaxation. The decay time of the diffusive mode can be tuned over a broad range of time scales by varying the reduced temperature ε , so that it may intersect the structural relaxation time, which is insensitive to the proximity to the critical point. As a consequence, it becomes possible to probe structural relaxation in complex fluids by dynamic light scattering of critical fluctuations. This method is an alternative to the traditional microrheology [7–9] that requires doping of probe particles in the fluid.

As an illustration of this principle, we have performed accurate light-scattering measurements of solu-

[†]This article was submitted by the authors in English.

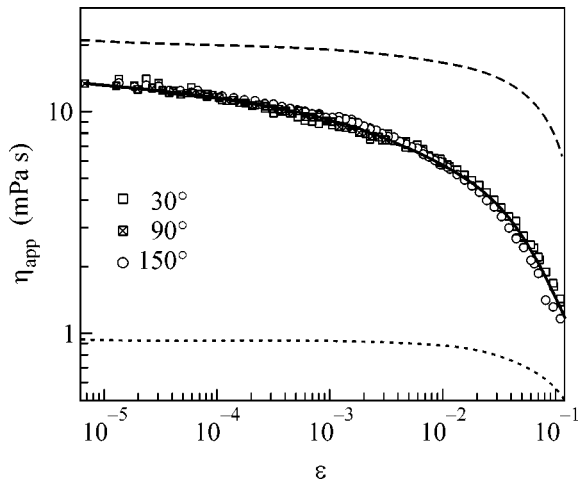


Fig. 1. Apparent mesoscopic viscosity of a solution of polystyrene ($M = 195, 900$) in cyclohexane as a function of $\varepsilon = (T - T_c)/T$ obtained by fitting the experimental light-scattering data to the mode-coupling theory. The dotted curve represents the viscosity of the solvent (cyclohexane), and the dashed curve represents the macroscopic viscosity of the same solution [12].

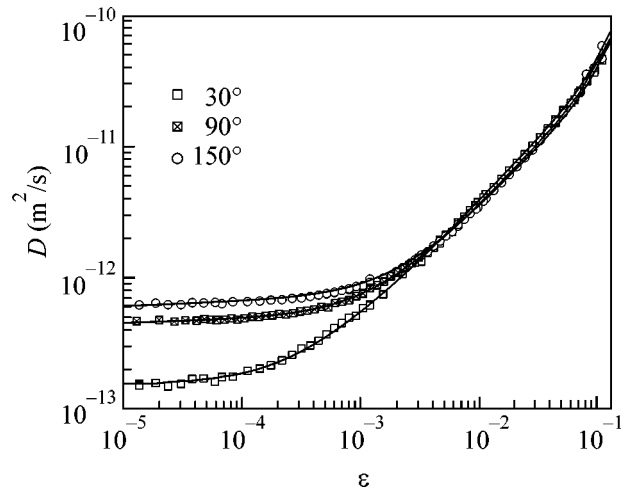


Fig. 2. Mesoscopic diffusion coefficient of a solution of polystyrene ($M = 195, 900$) in cyclohexane as a function of $\varepsilon = (T - T_c)/T$ measured at three scattering angles. The symbols represent experimental data, while the curves represent the critical contribution predicted by the mode-coupling theory with the mesoscopic viscosity shown in Fig. 1.

tions of nearly monodisperse polystyrene (with molecular weights M ranging from 10^4 to 10^7) in cyclohexane [10, 11]. The major result of our study is that the critical dynamics in polymer solutions appears to be very different from that in molecular fluids. Even for a modest polystyrene molecular weight of 195, 900, with the dynamic correlation function obeying a single-exponential decay, the apparent viscosity η_{app} extracted from dynamic light scattering (DLS) (on the basis of Eq. (2) with the correlation length ξ determined by static light scattering [10]) is vastly different from both the macroscopic viscosity of the solution and the viscosity of the solvent (Fig. 1). But, in terms of this apparent (“mesoscopic”) viscosity, the mesoscopic diffusion coefficient at various angles can be well described by Eq. (2) (lines through the symbols, Fig. 2). The pertinent question is: What is the physical meaning of this mesoscopic viscosity determined with DLS? Disagreements between the predictions of the mode-coupling theory for molecular fluids and the DLS data in near-critical polymer solutions have also been noted by others [12, 13] but have not yet been explained.

We have observed an even more dramatic change in dynamics in high-molecular-weight ($M = 10^6$ and higher) polymer solutions, where the dynamic correlation function turns out to deviate from a single-exponential decay and where two dynamic modes are clearly present. Far from the critical point, a fast mode dominates, while, close to the critical point, a slow mode dominates. Between these extremes, the data can be approximated by a sum of two exponentials, indicating contributions from both modes. The presence of two dynamic modes near the critical temperature

appears to be a universal feature in macromolecular systems and has been observed also by Ritzl *et al.* [14] for an $M = 1$ million polystyrene solution in cyclohexane and more recently by Tanaka *et al.* [15] for an $M = 4$ million polystyrene solution in diethyl malonate. These modes are effective dynamic modes, neither of which is purely viscoelastic (dictated by polymer chain dynamics) or purely diffusive (associated with the decay of critical fluctuations). Instead, the two observed modes emerge from a coupling of diffusive and viscoelastic modes, which belong to two different dynamic universality classes, pertaining to conserved and nonconserved order parameters [16]. The challenge is to quantitatively understand this coupled dynamic crossover behavior. A starting point in explaining the dynamics is the Brochard–De Gennes theory [17–19], which predicts a coupling of diffusion and chain relaxation in polymer solutions that has been subsequently detected experimentally in noncritical polymer solutions [20–22].

We submit that the Brochard–De Gennes theory can be applied to any system with dynamic coupling between conserved and nonconserved order parameters. Phenomenologically, it follows from this theory that the time-dependent intensity correlation function is the sum of two exponentials:

$$g_2(t) = 1 + \left\{ f_+ \exp\left[-\frac{t}{\tau_+}\right] + f_- \exp\left[-\frac{t}{\tau_-}\right] \right\}^2, \quad (3)$$

with the two decay times (slow τ_- and fast τ_+) and corresponding amplitudes (f_{\pm}) given by

$$\frac{1}{\tau_{\pm}} = \frac{1 + q^2 \xi_{ve}^2 + \frac{\tau_{ve}}{\tau_q} \pm \sqrt{\left(1 + q^2 \xi_{ve}^2 + \frac{\tau_{ve}}{\tau_q}\right)^2 - 4 \frac{\tau_{ve}}{\tau_q}}}{2\tau_{ve}}, \quad (4)$$

$$f_{\pm} = \frac{\frac{\tau_{ve}}{\tau_{\pm}} - (1 + q^2 \xi_{ve}^2)}{\frac{\tau_{ve}}{\tau_{+}} - \frac{\tau_{ve}}{\tau_{-}}}. \quad (5)$$

In Eq. (4), τ_{ve} is the q -independent viscoelastic relaxation time, τ_q is the q -dependent diffusion relaxation time, and ξ_{ve} is the mesoscopic viscoelastic length [23]. The above theory indeed grasps the essential features of our data (Figs. 3 and 4) if we use ξ_{ve} and τ_{ve} as adjustable parameters. In addition, to obtain $\tau_q = 1/Dq^2$, we need to use the apparent mesoscopic viscosity η_{app} in Eq. (2). The predictions for the two uncoupled modes (pure diffusion and pure viscoelastic relaxation) are indicated by the dashed curves in Fig. 3. While the diffusion relaxation time changes rapidly when the critical point is approached, the viscoelastic relaxation time exhibits a regular dependence on temperature. While the original uncoupled modes would cross each other at a certain temperature, the coupling produces two effective modes that “avoid crossing” each other very much similar to the well-known avoided crossing of two coupled energies [24]. Therefore, the microrheological characteristics can be deduced from scattering data in a near-critical fluid, since one can vary the diffusion relaxation time over many orders, thus probing the relevant viscoelastic times over the same range.

While ξ_{ve} (as expected [23, 25]) appears to be proportional to the viscosity, it was not clear *a priori* which viscosity is the appropriate quantity, the mesoscopic η_{app} or the macroscopic η at zero shear rate. Our study has shown that ξ_{ve} is proportional to the apparent (mesoscopic) viscosity measured by DLS. A further notable point is the shift in Fig. 3 between the calculated diffusion mode (long-dashed curve) and the observed slow mode (τ_- , solid curve). The data suggest

that τ_- is slowed down at nanoscales by a factor $q^2 \xi_{ve}^2$ with respect to the diffusion mode. For example, at $M = 11.4$ million and a scattering angle of 30° , where length scales of about $q^{-1} = 137$ nm are probed and ξ_{ve} reaches 200 nm, the slow mode is shifted from 0.4 to 1.5 s. We may attribute this anomalous slowing down of the fluctuations to “diffusion trapped by viscoelasticity at the nanoscale,” and we expect this effect to be ubiquitous in viscoelastic systems. Note that this effect of additional slowing down at smaller scales (large q) is opposite to the famous critical slowing down, which becomes more pronounced at larger scales (small q). In Fig. 4, the experimental amplitudes of these effective

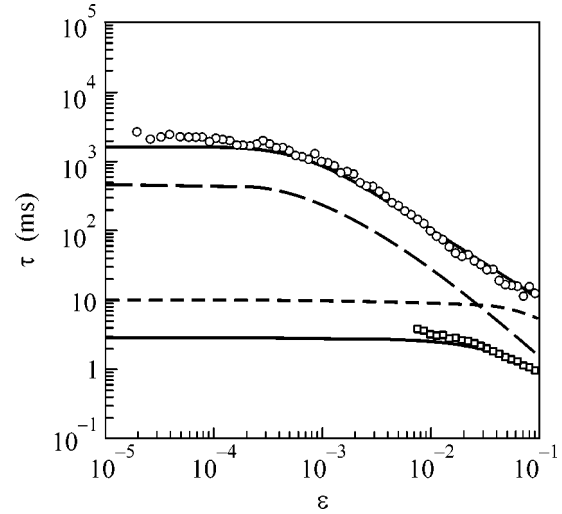


Fig. 3. Dynamic modes in a solution of polystyrene ($M = 11.4$ million) in cyclohexane for q , corresponding to a scattering angle of 30° . Open symbols represent the experimental relaxation times of the two observed modes. The solid curves represent the relaxation times of the effective “slow” and “fast” modes calculated with Eq. (4). The long-dashed curve represents the uncoupled critical-diffusion decay time. The short-dashed curve represents the uncoupled viscoelastic relaxation time.

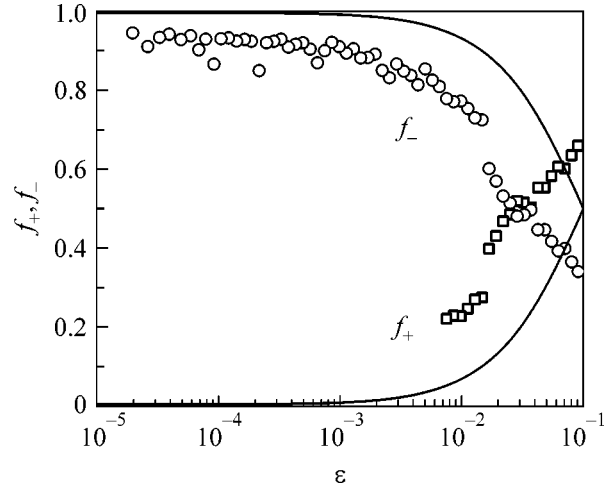


Fig. 4. Amplitudes of the two effective dynamic modes as a function of $\epsilon = (T - T_c)/T$ in a near-critical polymer solution. Solid curves are theoretical predictions for the amplitudes (Eq. (5)).

dynamic modes are compared with the theoretical ones calculated with Eq. (5). We submit that our interpretation of the coupled modes on the basis of the Brochard–De Gennes theory does account for the essential physics of the phenomenon. The analysis of the observed avoided crossing of two coupled modes has a good sensitivity because the amplitudes of the two effective

modes become of the same order of magnitude in the avoided-crossing domain (Fig. 4).

The key results obtained in our study are significant far beyond just the near-critical polymer solutions investigated. The coupling between diffusion-like and structure relaxation modes is expected whenever such modes are close to each other, and thus, scanning the diffusivity decay times by any means (varying composition, temperature, or pressure) will reveal the structural relaxation. Our results are relevant for a variety of complex fluids in which critical phenomena couple with a mesoscopic structure and/or viscoelastic relaxation. These include polymers in supercritical fluids [26], polymer blends [27], polymer solutions under shear [28], and microemulsions [29, 30], as well as systems important in the life sciences, such as solutions of polyelectrolytes or biopolymers [31, 32].

We conclude by highlighting the possible practical applications of studying the coupling between diffusive relaxation of critical fluctuations and structural relaxation. Because of this coupling, dynamic light scattering of critical fluctuations becomes a new tool for measuring the rheological properties of near-critical complex fluids. That is, by performing noninvasive DLS measurements on a sample, we can obtain quantitative information concerning its microrheological properties. Our proposed approach may be termed “critical microrheology” and does not require the addition of probe particles to the fluid. The uniqueness of critical microrheology is its ability to scan diffusive decay time of fluctuations at a given length scale q^{-1} over several orders of magnitude and, thereby, probe viscoelastic relaxation as an intrinsic fluid property. Moreover, instances have been reported where microrheological measurements are inconsistent with macroscopic rheology [33]. Critical microrheology experiments may clarify the nature and extent of these discrepancies. By selecting appropriate solvents for bringing systems into a near-critical state, one should be able to probe structural relaxation of a variety of macromolecular species in solutions.

We acknowledge some valuable discussion with M.R. Moldover. The research was supported by the Office of Basic Energy Sciences of the US Department of Energy (grant no. DE-FG-02-95ER-14509).

REFERENCES

1. H. L. Swinney and D. L. Henry, *Phys. Rev. A* **8**, 2586 (1973).
2. K. Kawasaki, in *Phase Transitions and Critical Phenomena*, Ed. by C. Domb and M. S. Green (Academic, New York, 1976), Vol. 5A, p. 165.
3. H. C. Burstin, J. V. Sengers, J. K. Bhattacharjee, and R. A. Ferrell, *Phys. Rev. A* **28**, 1567 (1983).
4. J. C. Nieuwoudt and J. V. Sengers, *J. Chem. Phys.* **90**, 457 (1989).
5. S. B. Kiselev and V. D. Kulikov, *Int. J. Thermophys.* **15**, 283 (1994).
6. J. Luettmmer-Strathmann, J. V. Sengers, and G. A. Olchowy, *J. Chem. Phys.* **103**, 7482 (1995).
7. T. G. Mason and D. A. Weitz, *Phys. Rev. Lett.* **74**, 1250 (1995).
8. T. Gisler and D. A. Weitz, *Curr. Opin. Colloid Interface Sci.* **3**, 586 (1998).
9. J. C. Crocker, M. T. Valentine, E. R. Weeks, *et al.*, *Phys. Rev. Lett.* **85**, 888 (2000).
10. M. A. Anisimov, A. F. Kostko, and J. V. Sengers, *Phys. Rev. E* **65**, 051805 (2002).
11. A. F. Kostko, M. A. Anisimov, and J. V. Sengers, *Phys. Rev. E* **66**, 020803(R) (2002).
12. Q. H. Lao, B. Chu, and N. Kuwahara, *J. Chem. Phys.* **62**, 2039 (1975).
13. B. M. Fine, J. Pande, A. Lomakin, *et al.*, *Phys. Rev. Lett.* **74**, 198 (1995).
14. A. Ritzl, L. Belkoura, and D. Woermann, *Chem. Phys.* **1**, 1947 (1999).
15. H. Tanaka, Y. Nakanishi, and N. Takubo, *Phys. Rev. E* **65**, 021802 (2002).
16. B. I. Halperin and P. C. Hohenberg, *Rev. Mod. Phys.* **49**, 435 (1977).
17. F. Brochard and P. G. De Gennes, *Macromolecules* **10**, 1157 (1977).
18. F. Brochard, *J. Phys. (Paris)* **44**, 39 (1983).
19. F. Brochard and P. G. De Gennes, *Physicochem. Hydrodyn.* **4**, 313 (1983).
20. M. Adam and M. Delsanti, *Macromolecules* **18**, 1760 (1985).
21. T. Jian, D. Vlassopoulos, G. Fytas, *et al.*, *Colloid Polym. Sci.* **274**, 1033 (1996).
22. T. Nicolai, W. Brown, R. M. Johnsen, *et al.*, *Macromolecules* **23**, 1165 (1990).
23. M. Doi and A. Onuki, *J. Phys. II* **2**, 1631 (1992).
24. L. D. Landau and E. M. Lifshitz, *Course of Theoretical Physics*, Vol. 3: *Quantum Mechanics: Non-Relativistic Theory*, 3rd ed. (Nauka, Moscow, 1974; Pergamon, New York, 1977).
25. A. Onuki, *Phase Transitions Dynamics* (Cambridge Univ. Press, Cambridge, 2002).
26. Y. B. Melnichenko, W. Brown, S. Rangelov, *et al.*, *Phys. Lett. A* **268**, 186 (2000).
27. H. Frielinghaus, D. Schwahn, J. Dudowicz, *et al.*, *J. Phys. Chem.* **114**, 5016 (2001).
28. P. K. Dixon, D. J. Pine, and X.-I. Wu, *Phys. Rev. Lett.* **68**, 2239 (1992).
29. J. Rouch, P. Tartaglia, and Sh. Chen, *Phys. Rev. Lett.* **71**, 1947 (1993).
30. T. Hellweg and R. von Klitzing, *Physica A (Amsterdam)* **283**, 349 (2000).
31. K. Nishida, K. Kaji, and T. Kanaya, *J. Phys. Chem.* **114**, 8671 (2001).
32. G. Chirico and G. Baldini, *J. Phys. Chem.* **104**, 6009 (1996).
33. J. H. Van Zanten and K. P. Rufener, *Phys. Rev. E* **62**, 5389 (2000).

Hybrids of Carbyne and Fullerene

A. R. Sabirov^{1,2}, I. V. Stankevich¹, and L. A. Chernozatonskii^{2,*}

¹ Nesmeyanov Institute of Organoelement Compounds, Russian Academy of Sciences, ul. Vavilova 28, Moscow, 119991 Russia

² Emanuel Institute of Biochemical Physics, Russian Academy of Sciences, ul. Kosygina 4, Moscow, 119991 Russia

*e-mail: cherno@sky.chph.ras.ru

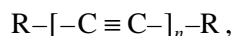
Received December 25, 2003

A new class of quasi-linear carbon molecules $[C_{60}]_n[C_m]_{n-1}$ consisting of n fullerenes C_{60} linked by $n-1$ carbyne-type C_m fragments with a system of conjugated bonds is described. The possible geometric configurations of such molecules and crystals on their base are discussed. The structure optimization by the empirical (MM+), semiempirical (PM3), and *ab initio* (HF/6-21) methods showed that these molecules are energetically stable.
© 2004 MAIK "Nauka/Interperiodica".

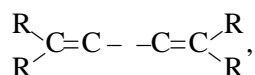
PACS numbers: 61.48.+c; 36.90.+f

The discovery of carbon allotropic forms such as carbyne, fullerenes, and nanotubes has stimulated investigations aimed at modeling the structures of new carbon materials and predicting their properties [1–6]. Inasmuch as carbon atoms can occur in one of the three hybrid states sp , sp^2 , and sp^3 , an infinite number of carbon crystalline forms can exist in practice. In these crystals, carbon atoms can have the same or different hybridization types and situate at surfaces of different topology. The possible existence of an infinitely large number of carbon crystal modifications was justified in [1] (see also reviews [2, 3]).

In this work, we discuss the possible existence of a new class of hybrid carbon structures consisting of fullerenes linked together by linear carbon fragments of the carbyne type. Recall that by the carbyne forms are meant carbon materials consisting mainly of carbon chains (see review [4]). Two types of molecules containing rather long linear carbon chains are presently known: polyynes ($RC_{2n}R'$) and cumulenes ($R_2C_nR_2$), where R and R' stand for the univalent atoms (e.g., H, F, Cl) or functional groups (e.g., CH_3 , C_6H_5). In the polyynes-type systems $RC_{2n}R$



the carbon fragment consists of the alternating single and triple bonds, and all carbon atoms are in the sp hybrid state. In the cumulene systems $R_2C_nR_2$



all C–C bonds are formally double, while the end carbon atoms are in the sp^2 hybrid state [1]. For this reason, free valence of each of them can be saturated by two functional groups or two univalent atoms. Note that the end groups CR_2 and CR'_2 in cumulenes with an odd

number of carbon atoms can be turned about each other by 90° .

In the cumulene systems, carbon atoms of one of the fullerene double bonds can serve as R and R' fragments. For this reason, the formation of the molecules consisting of two fullerenes, e.g., C_{60} , linked together only by a linear carbon chain of the cumulene type seems to be quite possible (Fig. 1).

Fullerene C_{60} contains six double bonds centered at the octahedron vertices. Consequently, fullerenes C_{60} can be linked together by carbyne chains to form quasi-one-dimensional (1D), quasi-two-dimensional (2D),

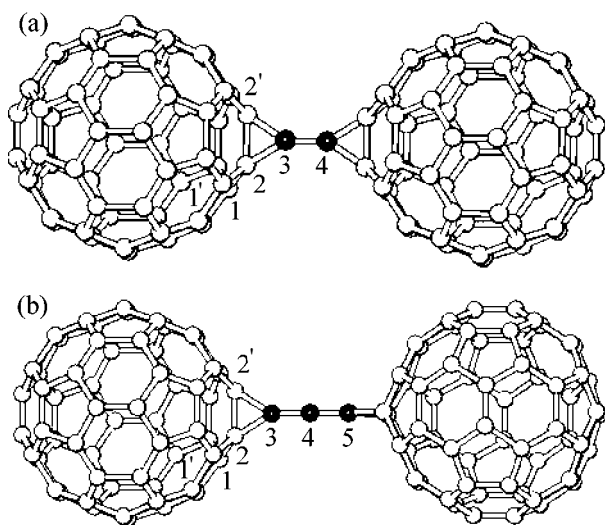


Fig. 1. Linkage between fullerenes through the carbyne chain: (a) $C_{60}C_2C_{60}$ and (b) $C_{60}C_3C_{60}$. Mutual geometric arrangement of the numbered atoms is given in Tables 1 and 2.

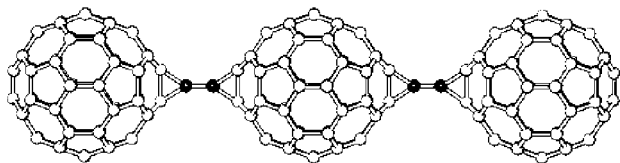


Fig. 2. Hybrid carbon cluster $[C_{60}]_3[C_2]_2$, which can be considered as a fragment of the $([C_{60}][C_2])_n$ polymer.

and three-dimensional (3D) crystal structures. In the quasi-two-dimensional structure, the chains can be bonded to fullerenes C_{60} in various ways. For this reason, no geometrical obstacles should arise to the formation of the same structures as those formed by the pure C_{60} polymers: orthorhombic (packed linear chains), tetragonal, and rhombohedral (packed layers) phases [6].

The purpose of this work is to assess the possibility of the existence for some monomeric and polymeric hybrid structures of carbyne and fullerenes. To this end, quantum-chemical calculations were carried out for hybrid carbon clusters consisting of two (Fig. 1) and three (Fig. 2) C_{60} fullerenes linked together by linear carbon chains with two to five C atoms and some of the 2D and 3D crystal structures on their base.

Dimers and trimers were calculated by the semiempirical PM3 method and the *ab initio* Hartree–Fock (HF/6-21G) method using the GAMESS program package for quantum-chemical calculations [7]. The 1D, 2D, and 3D crystal structures were calculated by the empirical molecular mechanic method (force field MM+; HYPERCHEM-6) in the cluster approximation.

The PM3 scheme is one of the parameterizations of the MNDO (modified neglect of differential overlap) method [8]. In this method, only valence electrons are considered and the overlap of atomic orbitals (AOs) belonging to different atoms is neglected, while the two-electron integrals of AOs belonging to the same atom are taken into account, allowing the interaction of

lone electron pairs to be taken into account more correctly than in other semiempirical methods.

In the *ab initio* method, the electron integrals are not replaced by empirical parameters, and the full self-consistent procedure is carried out with the calculation of all electron integrals. The basis set is taken in the form of AOs approximated by the Gaussian primitives. We used the split-valence (6-21G) basis; i.e., the core and valence orbitals were taken in the form of various sets of Gaussian primitives, which is necessary for a more accurate calculation of the electronic state in the presence of chemical bonding [8].

At present, these methods are widely used in the calculations of the fullerene and nanotube structures.

Computational results and discussion. The geometric structures of carbon clusters consisting of two fullerene molecules linked together by a linear carbon chain were calculated by full energy optimization of atomic coordinates. For the clusters containing three fullerene molecules, calculations were constrained to the D_{2h} symmetry to save run time. We found that the full optimization (without symmetry constraint) of clusters containing two fullerene molecules led to the same D_{2h} symmetry. The bond lengths and angles in the region where the linear fragments are bonded to fullerenes are given in Tables 1 and 2 (atomic numbering as in Fig. 1). For the structures with an odd number of carbon atoms in the linear fragment, the empirical and semiempirical methods predicted the existence of a stable state, in which the arrangement of all fullerenes about the symmetry axis going through the linear fragments is the same. However, the *ab initio* calculations showed that the configuration in which the fullerene fragments are alternately turned by 90° about the chain axis is the most stable.

The computational results obtained for the clusters containing three C_{60} fullerenes can be used to estimate the parameters of quasi-one-dimensional periodic structures consisting of an infinitely large number of alternating fullerenes and carbon chains and repeating elementary fragments of the form $C_{60}=C=C$,

Table 1. Bond lengths in the region of fullerene linkage (HF/6-21 calculations)

Type of molecule	Bond length, Å				
	1–2	2–2'	2–3	3–4	4–5
$[C_{60}]_2[C_2]$	1.492	1.629	1.461	1.287	–
$[C_{60}]_2[C_3]$	1.493	1.612	1.466	1.274	–
$[C_{60}]_2[C_4]$	1.493	1.614	1.465	1.279	1.258
$[C_{60}]_2[C_5]$	1.493	1.610	1.467	1.278	1.262
$[C_{60}]_3[C_2]_2$	1.492	1.629	1.460	1.286	–
$[C_{60}]_3[C_3]_2$	1.493	1.612	1.466	1.274	–
$[C_{60}]_3[C_4]_2$	1.493	1.614	1.465	1.279	1.258
$[C_{60}]_3[C_5]_2$	1.495	1.579	1.476	1.281	1.266

Table 2. Bond angles in the region of linkage between fullerene and cumulene (HF/6-21 calculations)

Type of molecule	Bond angle, deg			
	121'	123	232'	233'
[C ₆₀] ₂ [C ₂]	105.34	126.57	67.79	146.10
[C ₆₀] ₂ [C ₃]	105.36	126.41	66.69	146.69
[C ₆₀] ₂ [C ₄]	105.35	126.44	66.86	146.57
[C ₆₀] ₂ [C ₅]	105.35	126.40	66.56	146.72
[C ₆₀] ₃ [C ₂] ₂	105.33	126.58	67.84	146.08
[C ₆₀] ₃ [C ₃] ₂	105.29	126.43	66.68	146.66
[C ₆₀] ₃ [C ₄] ₂	105.31	126.45	66.86	146.57
[C ₆₀] ₃ [C ₅] ₂	105.13	126.19	64.69	147.65

Table 3. Main energy characteristics of the HF/6-21 structures: formation heats (ΔH_f), energies of dissociation into fullerenes and cumulenes (ΔE), and ionization energies (I)

Type of molecule	ΔH_f , kcal/(mol at.)	ΔE , kcal/(mol at.)	I , eV
[C ₆₀] ₂ "2 + 2"	13.22	0.42	
[C ₆₀] ₂ [C ₂]	13.78	1.80	8.01
[C ₆₀] ₂ [C ₃]	13.93	1.06	8.05
[C ₆₀] ₂ [C ₄]	14.07	2.23	7.99
[C ₆₀] ₂ [C ₅]	14.20	1.03	8.03
[C ₆₀] ₃ [C ₂] ₂	13.85	2.53	7.94
[C ₆₀] ₃ [C ₃] ₂	14.67	1.01	7.53
[C ₆₀] ₃ [C ₄] ₂	14.39	3.13	7.91
[C ₆₀] ₃ [C ₅] ₂	15.02	1.14	7.25

Table 4. Lattice parameters and strain energies of the crystal phases of C₆₀C₂ polymers according to the data for the central fragments of the MM+-optimized cluster structures (≤ 3000 atoms)

C ₆₀ C ₂ phase		a_1 , Å	a_2 , Å	a_3 , Å	E_{st} , kcal/(mol at.)
1D	Chain	11.12	–	–	10.96
2D	Orthorhombic, <i>Imm</i>	11.13	$a_2 = a_1$	–	16.45
	Hexagonal, $P\bar{6}m$	11.32	$a_2 = a_1$	–	18.50
3D	O phase, <i>Immm</i>	11.14	9.79	12.23	10.50
	T phase, <i>Immm</i>	11.11	$a_2 = a_1$	11.18	15.56
	Hexagonal, $P\bar{6}m2$	11.30	$a_2 = a_1$	13.83	17.70

C₆₀=C=C=C, etc. Note that the unit cell of a crystal formed by the fragments with an odd number of atoms is twice as large as the unit cell of a crystal with an even number of atoms in the chains between fullerenes. In this case, the atomic structure of a unit cell possesses the rotation-reflection symmetry about the chain axis and the plane passing perpendicular to this axis midway between the fullerenes; i.e., apart from the 90° rotation, fullerenes suffer no geometric changes.

The relative stability of the carbon hybrid structures was estimated using the differences in their formation heats (or total energies) and the formation heats of their fragments: C₆₀ fullerenes and C₂, C₃, C₄, and C₅ molecules (Table 3). It follows from the data given in this table that all configurations are energetically favorable and their stability is appreciably higher than for the [C₆₀]₂ dimer resulting from the [2 + 2] cycloaddition reaction [2, 6, 9]. It should be noted that the systems with an odd number of atoms in the cumulene frag-

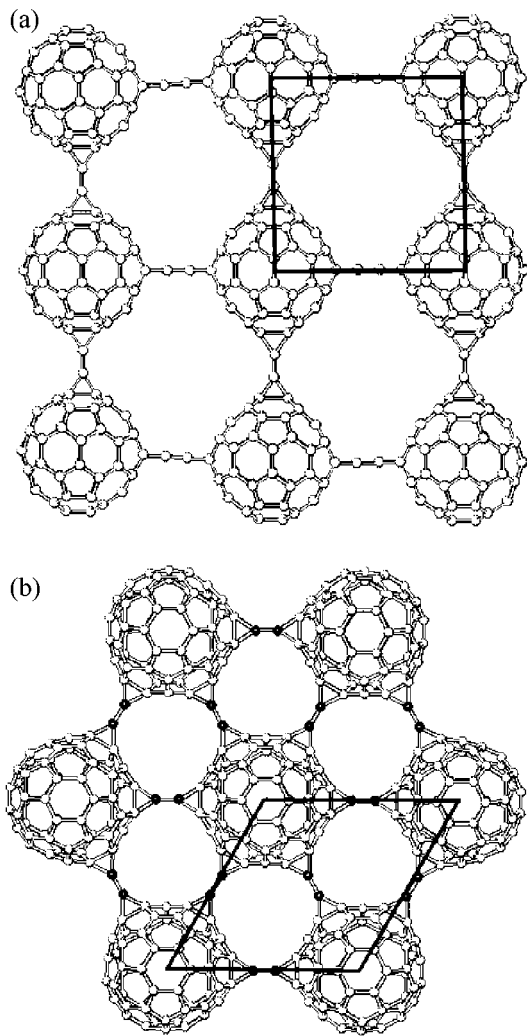


Fig. 3. Quasi-two-dimensional fullerene–cumulene crystals $C_{60}C_2$ with (a) rectangular and (b) hexagonal lattices. Straight lines indicate the crystal unit cells.

ments are much less stable than the analogous systems with an even number of atoms. One can also note that the stability of the systems with an even number of atoms increases both with the length of carbon chains and with the number of fullerene fragments.

The calculated ionization potentials of the molecules are given in Table 3. They are somewhat lower than for the C_{60} fullerene (7.63 eV [2]) and change only slightly on going from one molecule to another.

We also calculated the 1D, 2D, and 3D structures formed by chain-linked C_{60} fullerenes (Figs. 3, 4). The calculated fragment contained about 3000 atoms. The period of the chain (1D) structure ($a = 11.13 \text{ \AA}$) proved to be close to the *ab initio* molecular separation in the trimer (11.06 \AA). The related 3D O phase (by analogy with the polymeric C_{60} O phase [6]) with body-centered orthorhombic lattice of symmetry $Immm$ (Fig. 4a) is energetically more favorable than the 1D chain structure, as is seen from the comparison of their strain energies (Table 4). Of all the structures considered, this phase is the most stable. The unit cell parameter in the 2D structures (orthorhombic (Fig. 3a) and hexagonal (Fig. 3b)) is also close to 11.06 \AA . The corresponding phases (tetragonal T phase of symmetry $Immm$ (Fig. 4b) and hexagonal phase (Fig. 4c) of symmetry $P\bar{6}m2$) are also energetically more favorable than the 2D phases (Table 4).

Thus, energy estimates give grounds to believe that the formation of such structures is quite possible under the appropriate synthesis conditions, e.g., upon simultaneous evaporation of C_{60} and the carbon chain fragments C_2 , C_3 , C_4 , or C_5 .

Preliminary estimates show that the structures formed by these hybrids are semiconductors with a narrower energy gap than in the C_{60} crystals. Their electronic properties will be considered in a separate paper.

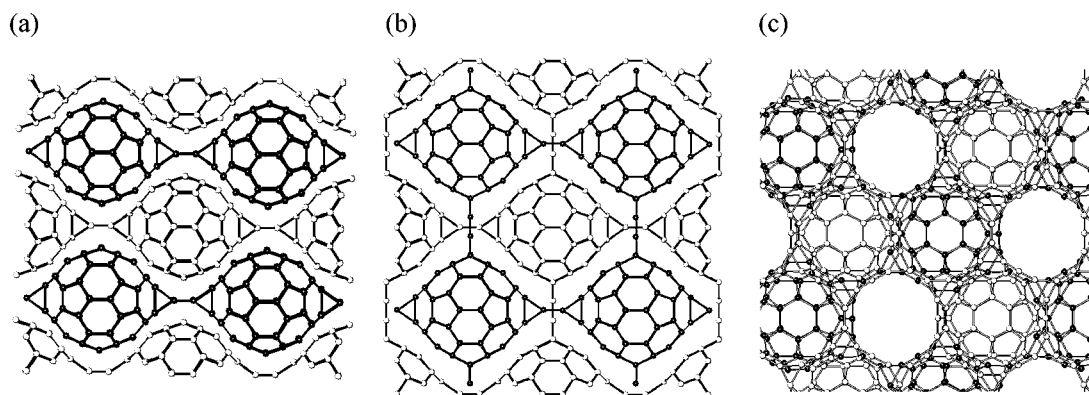


Fig. 4. 3D structures of crystal phases based on the fullerene–carbyne hybrids $C_{60}C_2$ (view in the [001] direction): (a) orthorhombic O, (b) orthorhombic T, and (c) hexagonal. The dark and light circles show, respectively, atoms of the molecules situated in the neighboring planes (001) and (001/2).

The large lattice parameters and the presence of double C–C bonds in the chain fragments allow these structures to be reliably identified among the polymeric C₆₀ phases, e.g., by the methods of electron paramagnetic resonance, X-ray structural analysis, Raman spectroscopy, etc.

This work was supported by the Russian Scientific and Technical Program “Controlled Synthesis of Fullerenes and Other Atomic Clusters.”

REFERENCES

1. I. V. Stankevich, M. V. Nikerov, and D. F. Bochvar, *Usp. Khim.* **7**, 1101 (1984).
2. M. S. Dresselhaus, G. Dresselhaus, and P. C. Eklund, *Science of Fullerenes and Carbon Nanotubes* (Academic, London, 1995).
3. U. H. F. Bunz, Y. Rubin, and Y. Tobe, *Chem. Soc. Rev.* **28**, 107 (1999).
4. Yu. V. Kudryavtsev, S. V. Evsyukov, M. B. Guseva, *et al.*, *Izv. Akad. Nauk, Ser. Khim.*, No. 3, 450 (1993).
5. V. I. Sokolov and I. V. Stankevich, *Usp. Khim.* **62**, 455 (1993).
6. M. Nunez-Regueiro, L. Marques, J.-L. Hodeau, *et al.*, *Phys. Rev. Lett.* **74**, 278 (1995).
7. M. W. Schmidt, K. K. Baldrige, J. A. Boatz, *et al.*, *J. Comput. Chem.* **14**, 1347 (1993).
8. N. F. Stepanov, *Quantum Mechanics and Quantum Chemistry* (Mir, Moscow, 2001).
9. M. Rao, P. Zhou, K.-A. Wang, *et al.*, *Science* **259**, 955 (1993).

Translated by V. Sakun

Magneto resonant Hardening of Silicon Single Crystals

Yu. A. Ossipyan¹, R. B. Morgunov^{1,*}, A. A. Baskakov¹, A. M. Orlov², A. A. Skvortsov²,
E. N. Inkina², and Y. Tanimoto³

¹*Institute for Solid State Physics, Russian Academy of Sciences, Chernogolovka, Moscow region, 142432 Russia*

*e-mail: morgunov@issp.ac.ru

²*Ul'yanovsk State University, Ul'yanovsk, 432970 Russia*

³*Institute for Molecular Science, 444-8585, Okazaki, Japan*

Received December 16, 2003; in final form, January 5, 2004

A microwave magnetic field crossed with a static field was found to exert a resonance effect on the dislocation mobility in single crystals of *p*-type silicon. The frequency of alternating field and the magnitude of static magnetic field corresponding to the maximal crystal hardening satisfy conditions for EPR of structural defects. This is evidence that the primary elementary processes observed previously in magnetoplasticity effects (influence of a static magnetic field on plasticity) are spin-dependent in silicon crystals. The dislocation path detected EPR spectrum was found to be anisotropic. © 2004 MAIK "Nauka/Interperiodica".

PACS numbers: 61.72.Hh

The studies of magnetic field (MF) effect on the mechanical properties of ionic crystals [1–10] have led to the revelation of crystal plasticization induced by electron paramagnetic resonance (EPR) of defect structures in crossed static and microwave magnetic fields [11]. This new physical phenomenon was predicted in [10]. More recently, the experimental results on magneto resonant crystal plasticization were confirmed and used as a new method for studying spin-dependent plasticity stages and for the indirect EPR detection during the process of plastic deformation [12–16]. It was established that the dislocation mean path [11, 12], the microhardness [13–15], and the strain hardening coefficient [16] of ionic crystals depend on the mutual spin orientation in the defect pairs, because it determines the efficiency of overcoming local obstacles (stoppers) by dislocations. The possibility of observing resonant crystal plasticization at near-room temperature is caused by the fact that the lifetimes of short-lived defect states are shorter than the spin relaxation time [11–16]. For this reason, an MF with a magnetic induction of ~1 T can influence both the paramagnetic impurity aggregation kinetics that determine the appearance of one or another type of dislocation stoppers [17–20] and the formation or rupture of the covalent bonds between a paramagnetic center situated at the dislocation line and a local obstacle in the bulk of ionic crystal [1–10].

To date, the EPR-stimulated change in plasticity was observed only in ionic crystals. However, it remains unclear whether the plasticity of other types of solids, e.g., those containing covalent bonds, can be affected by EPR. The answer to this question is of fundamental importance, because the possibility of selective frequency-tuned control of plastic deformation in crystals with various dislocation motion mechanisms

and various electronic structures would indicate the universal character of the role of spin in the formation of mechanical properties of crystals.

The dislocation mobility in Si single crystals (the most popular elementary semiconductor) is determined not only by local stoppers but also by the Peierls potential relief [21]. Some publications report that doped Si crystals containing dislocations become disordered after applying static MF with a magnetic induction of ~1 T [22–26]. However, the magnetoplastic effect in a static magnetic field alone does not necessarily signify that MF affects the dislocation mobility through the spin reorientation in Si defects. Although the magnetic field effect on the spin-dependent processes in the dislocation cores was already observed for silicon in [27, 28], the possibility of controlling its mechanical properties by switching mutual orientation of defect spins in a magnetic field have not been studied so far. It is the purpose of this work to study the dislocation mobility in *p*-type Si single crystals upon the simultaneous action of crossed static and microwave magnetic fields in the case where the ratio between the microwave frequency ν and the magnetic induction B_0 of a static MF satisfy the EPR condition $g\mu_B B_0 = h\nu$, where μ_B is the Bohr magneton, h is the Planck's constant, and $g \sim 2$ is the g factor.

Polished boron-doped silicon plates with a diameter of 100 mm and a resistivity of 1 Ω cm were grown by the Czochralski method and used in the experiment. After growth and polishing, the plates were protected from external action for several years. Samples of size 32 × 10 × 0.48 mm oriented in such a way that the large face corresponded to the (100) plane were cut from the plates perpendicularly to the main basic cut. This face

was used to make a scratch along the long crystal side parallel to the $[011]$ direction (Fig. 1). After this procedure, the sample was placed in a rectangular cavity matched to a magnetron at a constant frequency $\nu = 9.6$ GHz and situated between the electromagnet poles. An attenuator allowed the microwave power in the cavity to be adjusted within $P \sim 0.3 - 15$ W. After exposure to an MF for 30 min (at room temperature), the samples were taken out of the cavity and, after 30 min, deformed by four-point bending about the $[0\bar{1}1]$ direction at a temperature of 675°C . The reference samples were not subjected to magnetic fields and also kept for 33 min between the introduction of dislocations and the deformation. After the deformation, the (100) surface was subjected to a tension of 58 MPa that was constant along the crystal section under study and was the same in all experiments. According to [29], four dislocation glide systems were activated by this procedure: (111) $[\bar{1}\bar{1}0]$, (111) $[10\bar{1}]$, $(\bar{1}\bar{1}\bar{1})$ $[\bar{1}0\bar{1}]$, and $(\bar{1}\bar{1}\bar{1})$ $[110]$. As a result of sample loading at a temperature of 675°C , dislocation half-loops consisting of two 60-degree segments and a screw-dislocation fragment arranged parallel to the (100) surface appeared in the near-surface layer of the sample (Fig. 1).

After deformation, crystals were cooled to room temperature and chemically etched to locate the lines of dislocation outcrop at the surface using the standard set of reagents [22–25]. The paths of the 60-degree sections of frontal dislocations were measured using an optical microscope. Since the microwave amplitude in the cavity was not uniform along the sample length, each point for the B_0 dependence of the dislocation mean path L was obtained using a small section (with a size no greater than 5 mm) of the sample in the antinode of the microwave magnetic field. From three to four samples exposed to MF under the same conditions were used with the aim to accumulate sufficient statistics for the dislocation paths (~ 200 measurements) and provide a scatter of L no higher than 15% for each point in the graphs. Thus, the method of measurements was similar to the standard procedure of recording EPR spectra, except that the response to the resonance was detected not from the absorbed microwave power but from the dislocation paths and, instead of a continuous sweep of static MF, a discrete set of measurements with a step of ~ 0.1 T was carried out for different samples.

According to the data obtained by averaging over several samples, the dislocation mean path in crystals not exposed to MF was $L_0 = 300 \pm 15$ μm . This value was used as the reference point for measuring path increment after exposing crystals to MF. The quantity $(L - L_0)/L_0$, where L is the mean path of frontal dislocations after exposure to MF, was used as a measure of the MF effect on plasticity.

In the absence of a microwave field, $(L - L_0)/L_0$ increased monotonically with static MF directed along $[100]$ (Fig. 2, curve 1). That is, after exposure only to

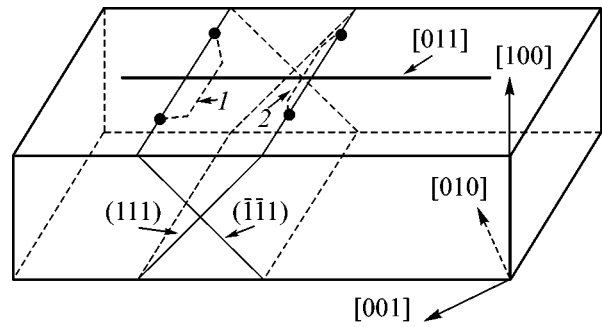


Fig. 1. Scheme illustrating the dislocation half-loops arisen in silicon single crystals near the (100) surface upon four-point bending about the $[0\bar{1}1]$ direction. Dislocation half-loops (1) and (2) are arranged in the glide planes (111) and $(\bar{1}\bar{1}\bar{1})$, respectively. Thick solid line indicates the scratch inscribed along the $[011]$ direction. The dislocation half-loop outcrops revealed by chemical etching of the (100) surface are shown by the black dots.

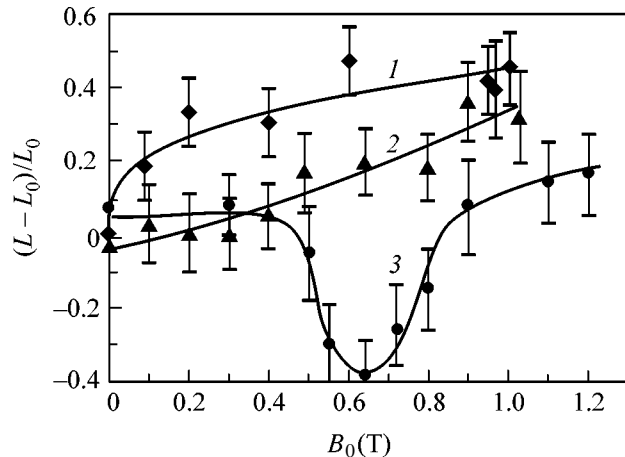


Fig. 2. The relative dislocation path under load vs. the induction of a static magnetic field B_0 applied before loading: (1) without microwave field; (2) in the presence of the static and microwave fields in the $B_0 \parallel B_1$ orientation; and (3) in the presence of the static and microwave fields in the $B_0 \perp B_1$ orientation. Microwave power in the cavity is ~ 0.3 W. In all experiments, $B_0 \parallel [100]$.

the static MF, crystals become disordered, much as it was reported earlier in [22–26]. In the presence of a microwave field with a power of $P \sim 0.3$ W, the $L(B_0)$ dependence changes radically. If the microwave magnetic component B_1 is perpendicular to the induction vector of the static MF $B_0 \parallel [100]$, $(L - L_0)/L_0$ depends on B_0 nonmonotonically. At $B_0 = 0.6$ T, it drastically decreases (by a factor of two), as compared to the experiments without the microwave field (Fig. 2, curve 3). Figure 3 presents the photographs of the reference

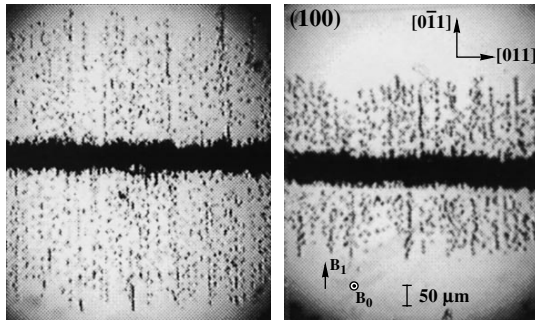


Fig. 3. Photographs of the Si (100) surfaces subjected to loading and chemical etching: (left) reference sample not exposed to MF and (right) a sample after the combined action of the static MF $B_0 = 0.6$ T and the microwave field in the $\mathbf{B}_1 \parallel \mathbf{B}_0$ orientation. In all experiments, $\mathbf{B}_0 \parallel [100]$ and the microwave power in the cavity is ~ 0.3 W.

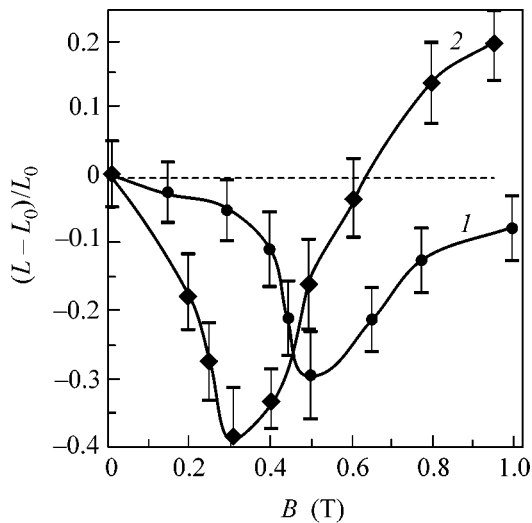


Fig. 4. The dislocation mean path under load vs. the induction of a static magnetic field $\mathbf{B}_0 \perp \mathbf{B}_1$ applied before loading in the (1) [100] direction and (2) $[0\bar{1}1]$ direction. The microwave power in the cavity is ~ 15 W.

sample and the sample exposed to the microwave and static fields in the conditions corresponding to the minimum of curve 3 in Fig. 2. For $\mathbf{B}_1 \parallel \mathbf{B}_0$, the B_0 dependence of the relative change in the dislocation path again becomes monotonic (Fig. 2, curve 2), but the corresponding curve lies slightly lower than the curve obtained in the absence of microwave field.

The study of the change in $(L - L_0)/L_0$ with changing position of the crystal section under study in the cavity showed that, at a fixed $B_0 = 0.6$ T, the maximal crystal hardening in the crossed static and microwave magnetic fields was achieved in the antinode of magnetic field.

The aim of the following types of measurements was to study the anisotropy of the resonant crystal hardening effect. Simultaneously, to reveal the role of the microwave power, it was chosen to be equal to ~ 15 W. The static and microwave magnetic fields were mutually perpendicular. Only the crystal orientation in the cavity was changed. For the $\mathbf{B}_0 \parallel [100]$ orientation, $(L - L_0)/L_0$ has a minimum near $B_0 = 0.5\text{--}0.6$ T, and the dislocation paths almost do not change upon a 50-fold increase in power (Fig. 4). However, for the $\mathbf{B}_0 \parallel [0\bar{1}1]$ orientation, the relative change in dislocation paths has a minimum at $B_0 = 0.3$ T (Fig. 4).

One of the main distinctions from the results obtained for ionic crystals [11–16] is that the dislocation paths in our experiments decrease, rather than increase, in the presence of static and microwave magnetic fields. The absence of resonant crystal hardening in the parallel orientation of the \mathbf{B}_1 and \mathbf{B}_0 vectors and the occurrence of hardening in the case of $\mathbf{B}_1 \perp \mathbf{B}_0$ unambiguously testifies that the spin transitions induced by EPR in the structural defects are the cause of the change in the dislocation mobility. It was established in the test experiments that crystal heating by $5\text{--}10^\circ\text{C}$ (instead of exposure to MF) does not change the dislocation paths upon the subsequent loading. The heating of the sample in the microwave field did not exceed 0.1°C . Therefore, the effect observed in this work at $P \sim 0.3$ W was not caused by mere crystal heating, so that it should be interpreted in terms of spin-dependent transitions in short-lived defect pairs.

The value $B_0 \sim 0.6$ T, for which the resonant hardening occurs in the $\mathbf{B}_0 \parallel [100]$ orientation in the case of $\mathbf{B}_1 \perp \mathbf{B}_0$, can be used to estimate the effective g factor $g_{[100]} \sim 1.1$ from the EPR condition $g\mu_B B_0 = h\nu$, where μ_B is the Bohr magneton and h is the Planck's constant. Contrary to ionic crystals [12–16], only a single resonance peak was observed in our experiments. This suggests that electron spins of the magnetically sensitive components of a defect pair are $S_e = 1/2$. The effective g factor in the case of $\mathbf{B}_0 \parallel [0\bar{1}1]$ orientation and $\mathbf{B}_1 \perp \mathbf{B}_0$ is $g_{[0\bar{1}1]} \sim 2.3$. A nearly twofold difference in the effective g factors ($g_{[100]} = 1.21$ and $g_{[0\bar{1}1]} \sim 2.43$) was observed earlier [30] in the standard EPR (i.e., detected from the absorption of microwave power) of a boron-doped p -type silicon. The fact that the g factors obtained in [30] from the data of standard EPR coincide with the values obtained in our work is evidence that boron atoms are incorporated into the magnetically sensitive defects, while the microwave-induced spin transitions in these defects are the primary processes causing magnetoresonant hardening.

As of now, one can hardly answer the question of the nature of magnetically sensitive defects in Si. Since the magnetoplastic effect was observed in [25] only for the silicon crystals grown by the Czochralski method and

was not for the Si crystals grown by the crucibleless melting, one can assume that, apart from the acceptor atoms, nonequilibrium oxygen complexes can be incorporated into the complexes under study. It is most likely that the transition to the nonequilibrium state in our experiments could occur at the stage of applying scratch with a local fracture of the material. It is well known that, in the oxygen atmosphere at room temperature, this process gives rise to numerous paramagnetic centers in the vicinity of the scratch [31].

The calculations of the binding energies of various boron complexes formed through chemical bonding to the (interstitial) silicon atoms indicate [32] that the binding energy of these complexes strongly depends on the boron charge state. As it changes (due to electron or hole capture), the complex transforms to the energetically more favorable state [32]. The atomic structure of the complexes formed upon the MF-sensitive structural relaxation can strongly influence the efficiency of overcoming these complexes, the starting stress, and, ultimately, the frontal dislocation path.

Magnetically sensitive complexes can form not only in the crystal bulk near the scratch but also in the dislocation cores arisen upon scratching, as well as near the surface of amorphous silicon. The nucleation of dislocation half-loops as a result of inscribing scratch at the (100) surface of *p*-type silicon was experimentally observed at room temperature by atomic force microscopy in [33].

In summary, magnetoresonant hardening of *p*-type silicon single crystals has been observed in crossed static and microwave magnetic fields. This is evidence that the structural relaxation of magnetically sensitive complexes responsible for the magnetoplastic effect in Si crystals is a spin-dependent process. The anisotropy observed for the resonance MF effect on the crystal plasticity characterizes the local symmetry of magnetically sensitive centers. The determination of atomic structure of the latter calls for further investigation.

We are grateful to Prof. V.V. Kveder for discussions and to Dr. Sci. (Phys.–Math.) S.Z. Shmurak for assistance in the experiment. This work was supported by the President Program for State Support of Leading Scientific School (project no. 00-15-96703) and Research of Young Doctors of Sciences (project no. MD-332.2003.02) and by the grant from FTsP Integratsiya (action 1.2, no. Z3418).

REFERENCES

1. V. I. Al'shits, E. V. Darinskaya, T. M. Perekalina, and A. A. Urusovskaya, *Fiz. Tverd. Tela (Leningrad)* **29**, 467 (1987) [*Sov. Phys. Solid State* **29**, 265 (1987)].
2. V. I. Al'shits, E. V. Darinskaya, and O. L. Kazakova, *Zh. Éksp. Teor. Fiz.* **111**, 615 (1997) [*JETP* **84**, 338 (1997)].
3. Yu. I. Golovin and R. B. Morgunov, *Pis'ma Zh. Éksp. Teor. Fiz.* **61**, 583 (1995) [*JETP Lett.* **61**, 596 (1995)].
4. V. I. Al'shits, N. N. Bekkauer, A. E. Smirnov, and A. A. Urusovskaya, *Zh. Éksp. Teor. Fiz.* **115**, 951 (1999) [*JETP* **88**, 523 (1999)].
5. N. A. Tyapunina, V. L. Krasnikov, and É. P. Belozerova, *Fiz. Tverd. Tela (St. Petersburg)* **41**, 1035 (1999) [*Phys. Solid State* **41**, 942 (1999)].
6. B. I. Smirnov, N. N. Peschanskaya, and V. I. Nikolaev, *Fiz. Tverd. Tela (St. Petersburg)* **43**, 2154 (2001) [*Phys. Solid State* **43**, 2250 (2001)].
7. N. V. Zagoruiko, *Kristallografiya* **10**, 81 (1965) [*Sov. Phys. Crystallogr.* **10**, 63 (1965)].
8. P. F. Biadzi, N. I. Gershenson, D. O. Zilpimiani, *et al.*, *Fiz. Tverd. Tela (Leningrad)* **32**, 2328 (1990) [*Sov. Phys. Solid State* **32**, 1352 (1990)].
9. E. V. Korovkin, *Pis'ma Zh. Éksp. Teor. Fiz.* **35**, 481 (1982) [*JETP Lett.* **35**, 595 (1982)].
10. M. Molotskii and V. Fleurov, *Philos. Mag. Lett.* **73**, 11 (1996).
11. Yu. I. Golovin and R. B. Morgunov, *Zh. Éksp. Teor. Fiz.* **115**, 605 (1999) [*JETP* **88**, 332 (1999)].
12. R. B. Morgunov, S. Z. Shmurak, A. A. Baskakov, and Y. Tanimoto, *Zh. Éksp. Teor. Fiz.* **124**, 840 (2003) [*JETP* **97**, 754 (2003)].
13. R. B. Morgunov, A. A. Baskakov, I. N. Trofimova, and D. V. Yakunin, *Fiz. Tverd. Tela (St. Petersburg)* **45**, 257 (2003) [*Phys. Solid State* **45**, 270 (2003)].
14. Yu. I. Golovin, R. B. Morgunov, and A. A. Dmitrievskii, *Mater. Sci. Eng.* **115**, 345 (2000).
15. Yu. I. Golovin, R. B. Morgunov, and A. A. Baskakov, *Mol. Phys.* **100**, 1291 (2002).
16. Yu. I. Golovin, R. B. Morgunov, V. E. Ivanov, and A. A. Dmitrievskii, *Zh. Éksp. Teor. Fiz.* **117**, 1080 (2000) [*JETP* **90**, 939 (2000)].
17. R. B. Morgunov and A. A. Baskakov, *Fiz. Tverd. Tela (St. Petersburg)* **43**, 1632 (2001) [*Phys. Solid State* **43**, 1700 (2001)].
18. R. B. Morgunov, S. Z. Shmurak, A. A. Baskakov, *et al.*, *Pis'ma Zh. Éksp. Teor. Fiz.* **76**, 366 (2002) [*JETP Lett.* **76**, 307 (2002)].
19. R. B. Morgunov and A. A. Baskakov, *Fiz. Tverd. Tela (St. Petersburg)* **45**, 91 (2003) [*Phys. Solid State* **45**, 94 (2003)].
20. R. B. Morgunov, S. Z. Shmurak, A. A. Baskakov, and Y. Tanimoto, *Phys. Status Solidi B* **135**, 276 (2004).
21. V. I. Nikitenko and Yu. A. Osip'yan, in *Problems in Modern Crystallography*, Ed. by B. K. Vainshtein and A. A. Chernov (Nauka, Moscow, 1975), p. 239.
22. I. I. Soloshenko and A. F. Zolotarev, in *Mechanisms of Internal Friction in Semiconductor and Metallic Materials* (Nauka, Moscow, 1972), p. 35.
23. V. A. Makara, L. P. Steblenko, N. Ya. Gorid'ko, *et al.*, *Fiz. Tverd. Tela (St. Petersburg)* **43**, 462 (2001) [*Phys. Solid State* **43**, 480 (2001)].
24. A. M. Orlov, A. A. Skvortsov, and A. A. Solov'ev, *Zh. Éksp. Teor. Fiz.* **123**, 590 (2003) [*JETP* **96**, 523 (2003)].

25. A. A. Skvortsov, A. M. Orlov, and L. I. Gonchar, *Zh. Éksp. Teor. Fiz.* **120**, 134 (2001) [*JETP* **93**, 117 (2001)].
26. M. V. Badylevich, Yu. L. Iunin, V. V. Kveder, *et al.*, *Zh. Éksp. Teor. Fiz.* **124**, 664 (2003) [*JETP* **97**, 601 (2003)].
27. V. V. Kveder and Yu. A. Osip'yan, *Zh. Éksp. Teor. Fiz.* **80**, 1206 (1981) [*Sov. Phys. JETP* **53**, 618 (1981)].
28. Yu. A. Osip'yan, S. I. Bredikhin, V. V. Kveder, N. V. Klassen, V. D. Negrii, V. F. Petrenko, I. S. Smirnova, S. A. Shevchenko, S. Z. Shmurak, and É. A. Shteinman, *Electronic Properties of Dislocations in Semiconductors* (Éditorial URSS, Moscow, 2000).
29. M. V. Mezhennyi, M. G. Mil'vidskii, and V. Ya. Reznik, *Fiz. Tverd. Tela* (St. Petersburg) **44**, 1224 (2002) [*Phys. Solid State* **44**, 1278 (2002)].
30. G. Feher, J. C. Hensel, and E. A. Gere, in *Electron Spin Resonance in Semiconductors*, Ed. by N. A. Penin (Inostrannaya Literatura, Moscow, 1962), p. 111.
31. M. V. Vlasova and N. G. Kakazei, *Electron Paramagnetic Resonance in Failed Solids* (Naukova Dumka, Kiev, 1979), p. 66.
32. J. Jeong and A. Oshiyama, *Phys. Rev. B* **64**, 235204 (2001).
33. J. Rabier, R. Cordier, T. Tondellier, *et al.*, *J. Phys.: Condens. Matter* **12**, 1059 (2000).

Translated by V. Sakun

Decrease in the Bond Energy of Arsenic Atoms on the GaAs(100)-(2 × 4)/c(2 × 8) Surface Due to the Effect of Adsorbed Cesium

O. E. Tereshchenko, V. L. Alperovich, and A. S. Terekhov

Institute of Semiconductor Physics, Siberian Division, Russian Academy of Sciences, Novosibirsk, 630090 Russia
Novosibirsk State University, Novosibirsk, 630090 Russia

Received January 8, 2004

It has been found experimentally that the bond energy of arsenic atoms on the GaAs(100) surface decreases under the influence of adsorbed cesium. This is manifested in the disordering of the As-stabilized surface and in a decrease of ~100 K in the temperature of the transition to the Ga-stabilized (100)GaAs(4 × 2)/c(8 × 2) surface. This effect is caused by the redistribution of the valence electron density between the arsenic atoms in the upper layer and the gallium atoms in the lower-lying layer as a result of charge transfer from the electropositive adsorbate to the semiconductor. In combination with the analogous effect of a decrease in the bonding energy of gallium atoms on the Ga-stabilized GaAs surface upon the adsorption of electronegative adsorbates (halogens), the effect observed allows the atomic layer etching of the polar GaAs(100) face. © 2004 MAIK "Nauka/Interperiodica".

PACS numbers: 68.35.-p; 81.15.Ef

Advances in the physics of low-dimensional systems, which has been intensively developed in recent years, are closely related to the capabilities of modern epitaxial technologies such as atomic layer epitaxy [1]. These capabilities are such that heterostructures and superlattices in which the layer thicknesses and interface smoothness are controlled to an accuracy of one monolayer. Not only atomic layer growth proves to be necessary for modern nanotechnology, but the atomic layer etching of semiconductors turns out to be necessary as well. Atomic layer etching represents precision crystal disassembling by removing monolayers one by one with the retention of the atomic smoothness of the surface. Atomic layer etching with a resolution of one monolayer can be accomplished apparently on polar faces of binary III–V compound semiconductors by using adsorbates that selectively react with atoms of the third and fifth groups. It has been shown in [2, 3] that the adsorption of iodine on an atomically pure Ga-stabilized GaAs(100) surface is accompanied by its preferential bonding to gallium atoms. The low-temperature heating of the iodinated surface leads to the desorption of reaction products in the form of GaI_x and to the formation of the (2 × 4)-reconstructed As-terminated surface. Similar results were obtained for the adsorption of various halogens on III–V semiconductors [2, 4]. The selectivity of the chemical activity of halogens to a third group element suggested that alkali metals can selectively weaken the bond of fifth group atoms on the surface of III–V semiconductors. The goal of this work was to examine the possibility of decreasing the temperature of arsenic desorption from the

GaAs(100) surface under the influence of the adsorption of an electropositive adsorbate, namely, an alkali metal.

To exclude the possible effect of defects in the disturbed surface layer of GaAs wafers on the stoichiometry and structure of the surface, the experiments were carried out with epitaxial GaAs(100) layers. The preparation of the pure GaAs surface involved the removal of oxides with a solution of HCl in isopropyl alcohol (IPA) in a dry nitrogen atmosphere, after which the sample was transferred to an ADES-500 ultrahigh-vacuum electronic spectrometer in a hermetically sealed container without contact with air, followed by its vacuum heating [5]. The structure and chemical composition of the surface were determined by low-energy electron diffraction (LEED) and X-ray photoelectron spectroscopy (XPS), respectively. Cesium was used as the electropositive adsorbate. The deposition of Cs was carried out in the preparation chamber of the spectrometer under a vacuum of 10⁻¹⁰ mbar using dispensers filled with purified cesium chromate. The temperature of Cs dispensers did not exceed 500°C. The time interval between the deposition of Cs and the measurement of its concentration in the analytical chamber was about 5 min. The deposition of Cs and all measurements were performed at room temperature.

As the first step of comparative study of the variation of the properties of As- and Ga-stabilized surfaces of the polar GaAs(100) face upon Cs adsorption, we measured the dose dependences of the amount of Cs adsorbed on these surfaces by XPS. Because the thick-

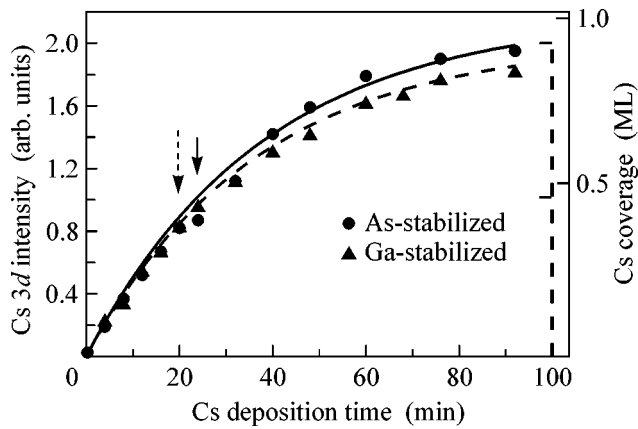


Fig. 1. Dependences of the Cs3d photoemission peak area on the time of Cs deposition onto the As-stabilized GaAs(100)-(2 × 4)/c(2 × 8) surface (circles) and Ga-stabilized GaAs(100)-(4 × 2)/c(8 × 2) surface (triangles). Solid and dashed curves correspond to the dependences calculated within the Langmuir adsorption model for the As- and Ga-stabilized surfaces, respectively. Cs coverages θ in monolayers for these surfaces are shown by the solid and dashed lines in the ordinate axis on the right-hand side. The solid and dashed arrows indicate the time t_{\max} that corresponds to the maximum photoemission on the As- and Ga-stabilized surfaces, respectively.

ness of the adsorbed Cs layer at room temperature (in the absence of a Cs flow) does not exceed one monolayer (ML) [6], the concentration of Cs atoms on the surface was assumed to be directly proportional to the integral intensity A of the photoemission Cs3d line excited by the X-ray AlK_{α} line at 1486 eV. The work function measured during the deposition of Cs was monitored by measuring the electron emission current into a vacuum upon illumination by a semiconductor laser ($\lambda = 655$ nm). A maximum of photoemission from the As-stabilized surface was achieved in the time $t_{\max} = 25$ min, and that from the Ga-stabilized surface was achieved in 19 min.

The results of measuring the dependence of the Cs3d peak area on the cesium deposition time $A(t)$ for GaAs(100) surfaces with different stoichiometries are shown in Fig. 1. It is evident in the figure that the dependences $A(t)$ measured for the As- and Ga-stabilized surfaces with (2 × 4)/c(2 × 8) and (4 × 2)/c(8 × 2) superlattices, respectively, are rather close to each other. According to the scatter of the experimental points, the systematic differences in the amount of cesium observed at $t \geq 40$ min exceed the random error but lie within the limits of the absolute error of the XPS technique, which is equal to $\sim 10\%$. It is also evident that the linear growth of the cesium concentration observed for small doses ($t < t_{\max}$) slows down and subsequently goes to saturation at large doses ($t > t_{\max}$). This behavior is in agreement with the results obtained previously by Auger spectroscopy for Cs adsorption on

the Ga-stabilized GaAs(100) surface [7–9]. To perform a quantitative analysis of the obtained dependences, we used the Langmuir adsorption model [7], in which it is assumed that the probability that an atom will be adsorbed on the surface is proportional to the sticking coefficient α and to the concentration of the unoccupied adsorption sites. For a constant Cs flux density, the Langmuir model gives the following form of the dependences $A(t)$ and the coverage $\theta(t)$:

$$A(t) = A_0\theta(t); \quad \theta(t) = 1 - \exp\left(-\frac{\alpha R t}{N_0}\right), \quad (1)$$

where α is the sticking coefficient of adatoms on a clean surface; N_0 is the concentration of adatoms in one monolayer, which equals $N_0 \approx (6 - 8) \times 10^{14}$ atoms/cm² [7] for a cesium monolayer; R is the density of the adatom flux onto the surface, which was constant in our experiments to within 5%; $A_0 = kN_0$ is the Cs3d peak area at saturation; and k is a constant depending on the element sensitivity factor for cesium and on the X-ray radiation intensity, which was also maintained constant. The solid and dashed lines indicate the Langmuir adsorption curves that are calculated by Eq. (1) using the least-squares method and describe the experimental data for the As- and Ga-stabilized surfaces, respectively. Figure 1 demonstrates that the experimental data for both surfaces are described well within the Langmuir model with coefficients α independent of the coverage θ . From the obtained values of fitting parameters A_0 and $t_0 = N_0/\alpha R$, it follows that the values of α for the As- and Ga-stabilized GaAs(100) surfaces coincide to within 4%, that is, within the experimental error. According to [10, 11], the sticking coefficient of Cs on the Ga-stabilized surface is close to unity. Therefore, as follows from the data obtained in this work, $\alpha \approx 1$ for the As-stabilized surface as well, in contradiction to the conclusions made by the authors of [12]. In connection with this contradiction, we emphasize that no direct measurement of the amount of cesium on the surface was performed in [12]. Thus, the sticking coefficient of cesium on the GaAs(100) surface is close to unity and does not depend on its stoichiometry or structure.

We continued to search for the selectivity of cesium interaction with the As- and Ga-stabilized GaAs(100) surfaces by studying the effect of cesium adsorption on the structure of these surfaces. For this purpose, LEED patterns were measured for clean surfaces with different stoichiometries and for these surfaces upon cesium deposition. The results are shown in Fig. 2. The clean surfaces with an As-stabilized (2 × 4)/c(2 × 8) superlattice (Fig. 2a) and with a Ga-stabilized (4 × 2)/c(8 × 2) superlattice (Fig. 2d) were obtained by removing oxides in an IPA solution of HCl followed by heating in vacuum at temperatures $T = 450$ and 560°C , respectively. The deposition of cesium on the As-stabilized surface leads to a rapid smearing of the diffraction pattern, which points to a disordering of the surface. The intensity of diffraction reflections with respect to the

background of diffusely scattered electrons decreases several times already at the coverage $\theta \sim 0.1$ ML, while the fractional reflections disappear at $\theta \approx 0.3\text{--}0.5$ ML (Fig. 2b). An increase in θ to 0.7 ML leads to the disappearance of part of the main reflections as well, whereas the intensity of the remaining reflections becomes several times lower than the diffuse background. On the other hand, Cs on the Ga-stabilized surface is adsorbed significantly more orderly: the $(4 \times 2)/c(8 \times 2)$ structure is clearly visible at $\theta = 0.5$ ML (Fig. 2e) and is retained up to $\theta \approx 0.75$ ML. With a further increase in the coverage, the fractional reflections disappear and the diffuse background increases. Nevertheless, at $\theta \sim 1$ ML, the (1×1) diffraction pattern for the Ga-stabilized surface remains significantly more distinct than for the As-stabilized surface.

By and large, the results obtained are in agreement with the statement made by the authors of [6, 13] that the low-energy electron diffraction pattern degrades upon cesium diffraction and a disordered Cs/GaAs(100) boundary forms. However, though it was stated in [6] that this process proceeds similarly for both the As- and Ga-stabilized GaAs(100) surfaces, there is no data in the literature that would allow us to compare the evolution of the structure of these surfaces upon an increase in the cesium coverage. As follows from the results obtained in this work, there are significant differences in the action of cesium on the structure of the As- and Ga-stabilized surfaces. These differences are caused not by different sticking coefficients but by the fundamental differences in the adsorption mechanism. The differences in the structure of the Cs/GaAs interfaces depending on the starting reconstruction are most pronounced in the experiments on heating cesium-coated surfaces. Figures 2c and 2f demonstrate LEED patterns after coating the As- and Ga-stabilized surfaces with cesium up to $\theta \sim 1$ ML followed by heating at temperatures of 470 and 450°C, respectively. After heating, the residual amount of cesium on the surface is $\theta \leq 0.1$ ML. It is seen in Fig. 2c that cesium adsorption and heating lead to the conversion of the As-stabilized $(2 \times 4)/c(2 \times 8)$ surface into the Ga-stabilized $(4 \times 2)/c(8 \times 2)$ surface, and the conversion proceeds starting with the heating temperature $T = 450^\circ\text{C}$. On the contrary, the Ga-stabilized $(4 \times 2)/c(8 \times 2)$ structure destroyed by the deposition of 1 ML of Cs is restored by heating at temperatures $T \geq 200^\circ\text{C}$.

The effect of the cesium-induced conversion of the As-stabilized surface to the Ga-stabilized one detected in this work seems interesting and important. It is known that the As-stabilized GaAs(100)- $(2 \times 4)/c(2 \times 8)$ superlattice is reproducibly obtained by heating at $T = 420\text{--}480^\circ\text{C}$ [5, 14]. It is more complicated to obtain the ordered Ga-stabilized $(4 \times 2)/c(8 \times 2)$ surface, because to do this requires heating to temperatures 560–600°C. These temperatures are close to the incongruent evaporation temperature of GaAs, at which many point defects are generated in the near-surface region, the

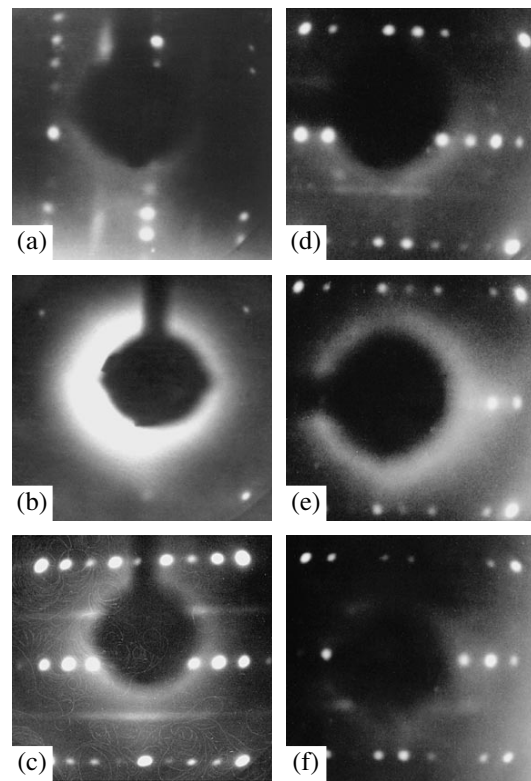


Fig. 2. LEED patterns upon Cs adsorption on (left-hand column, (a), (b), and (c)) the As-stabilized surface and (right-hand column, (d), (e), and (f)) Ga-stabilized GaAs(100) surfaces followed by heating. Patterns (a) and (d) were obtained on pure substances with $(2 \times 4)/c(2 \times 8)$ and $(4 \times 2)/c(8 \times 2)$ superlattices, patterns (b) and (e) were obtained after the deposition of cesium (0.5 ML) onto these surfaces, and patterns (c) and (f) were obtained after heating at 470 and 450°C, respectively.

morphology of the surface deteriorates, and the occurrence of even submonolayer impurities leads to its faceting [15]. The sequence of Figs. 2a–2c illustrates an alternative method for obtaining the $(4 \times 2)/c(8 \times 2)$ superlattice at a lower temperature ($T = 450\text{--}470^\circ\text{C}$) using cesium preadsorption.

To elucidate the reasons for the cesium-induced disordering of the As-stabilized $(2 \times 4)/c(2 \times 8)$ superlattice and the decrease in the temperature of the phase transition to the Ga-stabilized $(4 \times 2)/c(8 \times 2)$ superlattice, we will compare these effects with the known results on the effect of electronegative adsorbates (halogens) on the surface stoichiometry and structure of III–V semiconductors [2–4]. It was shown in [2, 3] that the adsorption of iodine onto a Ga-rich GaAs(100)- $(4 \times 2)/c(8 \times 2)$ surface followed by heating results in a structurally ordered As-rich surface with a $(2 \times 4)/c(2 \times 8)$ superlattice. At the same time, the adsorption of iodine followed by the heating of the As-stabilized surface does not change its starting composition or structure.

The transformations of the surface structure under the action of both cesium and iodine are caused by the change of its stoichiometry due to the removal of part of the atoms of the upper layer: the cesium-induced transition is due to the removal of arsenic atoms, and the iodine-induced transition is due to the removal of gallium atoms. In turn, the adatom-induced removal of surface atoms depends primarily on whether the bonds of atoms of the upper layer with atoms of the second layer (so-called backbonds) become weaker or stronger. It is known that the stabilization of the main surface reconstructions of III–V semiconductors and the corresponding strengthening of bonds on the surface is attained through the transfer of electrons from the partially occupied dangling bonds of the cation to the orbitals of the anion, so that the orbitals of the anion become fully occupied, while those of the cation become empty [16]. Therefore, it can be suggested that the destabilization of a superlattice and the weakening of backbonds occur in the case when adsorption induces the return of electron density from anions to cations. This suggestion explains the opposite action of cesium and iodine with regard to the differences in the electronegativity of these elements. In the case of adsorption of electropositive cesium atoms on the As-stabilized GaAs(100) surface, the electron-density transfer from cesium to the upper layers of GaAs leads to the return of electron density from arsenic to lower-lying gallium. This leads to a weakening of backbonds and, as a result, to the disordering of the As-stabilized surface and to a decrease in the temperature of the transition to the Ga-stabilized surface, as was observed in this work. Analogous considerations for the electronegative adsorbate (iodine) lead to the conclusion that the backbonds become weaker upon adsorption on the Ga-stabilized surface, which is favorable to the transition to the As-stabilized surface upon the subsequent low-temperature heating [2, 3].

It should be emphasized that the suggested explanation based on the symmetry of charge transfer from adatoms to a semiconductor is of a solely qualitative character and does not take into account significant differences in the character of cesium and iodine interactions with the surface. In particular, it is known that chemically shifted components induced by chemisorption are distinctly visible in the photoemission lines of Ga and As on the I_2 /GaAs surface [2], while the data on the presence or absence of chemically shifted components on the Cs/GaAs surface are ambiguous [17, 18]. Note also that other halogens (F, Cl, and Br) and alkali metals (Na, K, and Rb) with lower atomic numbers and smaller covalent radii lead to cruder effects, in particular, to the steady etching of the surface by halogens and to clusterization of alkali-metal adatoms due to their higher chemical activity in the interaction with the surface of III–V semiconductors, as compared with cesium and iodine. On the contrary, cesium and iodine

are elements with large covalent radii. Therefore, they participate in more subtle and selective interactions that depend on the composition and structure of the starting surface, which provides the possibility of low-temperature adatom-induced reconstruction transitions and atomic layer etching.

Thus, it has been shown in this work that the changes in the atomic structure of GaAs(100) surfaces with different stoichiometries that occur upon the adsorption of submonolayer cesium coatings are substantially different; the As-stabilized surface with the $(2 \times 4)/c(2 \times 8)$ superlattice becomes disordered at considerably smaller coverages compared with the Ga-stabilized surface with the $(4 \times 2)/c(8 \times 2)$ superlattice, though the sticking coefficients of Cs atoms on the As- and Ga-stabilized GaAs(100) surfaces coincide within the accuracy of the XPS technique. This observation indicates that charge transfer from cesium adatoms to the semiconductor weakens the chemical bonds of arsenic atoms. An additional corroboration of this conclusion is the cesium-induced decrease of $\sim 100^\circ\text{C}$ in the temperature of the reconstruction transition from the As-stabilized surface to the Ga-stabilized one observed in this work. Along with the known phenomenon of a decrease in the bonding energy of Ga atoms due to the adsorption of iodine on the Ga-stabilized GaAs(100) surface [2, 3], this effect opens up possibilities for the low-temperature ($T \leq 450^\circ\text{C}$) atomic layer etching of polar faces of III–V compounds.

This work was supported by the Russian Foundation for Basic Research (project no. 01-02-17694), the Ministry of Education of the Russian Federation, program Integration (project no. I765/785), the Ministry of Industry, Science, and Technology of the Russian Federation, program Surface Atomic Structures (project no. 40.012.1.1.1151), and the Russian Academy of Sciences, program Spin-Dependent Effects in Solids and Spintronics.

REFERENCES

1. M. Ritala and M. Leskelä, *Nanotechnology* **10**, 19 (1999).
2. P. R. Varekamp, M. C. Häkansson, J. Kanski, *et al.*, *Phys. Rev. B* **54**, 2101 (1996).
3. K. N. Eltsov, V. M. Shevlyuga, and A. A. Vedenev, in *Proceedings of International Conference on Scanning Probe Microscopy (SPM-2002)* (Nizhni Novgorod, Russia, 2002), p. 99.
4. W. K. Wang, W. C. Simpson, and J. A. Yarmoff, *Phys. Rev. Lett.* **81**, 1465 (1998); *Phys. Rev. B* **61**, 2164 (2000).
5. O. E. Tereshchenko, S. I. Chikichev, and A. S. Terekhov, *J. Vac. Sci. Technol. A* **17**, 2655 (1999).
6. B. Goldstein, *Surf. Sci.* **47**, 143 (1975).
7. D. L. Smith and D. A. Huchital, *J. Appl. Phys.* **43**, 2624 (1972).

8. D. Rodway, Surf. Sci. **147**, 103 (1984).
9. G. Vergara, L. J. Gómes, J. Capmany, and M. T. Montojo, Surf. Sci. **278**, 131 (1992).
10. M. Kamaratos and E. Bauer, J. Appl. Phys. **70**, 7564 (1991).
11. A. J. van Bommel, J. E. Crombeen, and T. G. J. van Oirschot, Surf. Sci. **72**, 95 (1978).
12. G. V. Benemanskaya, D. V. Daineka, and G. E. Frank-Kamenetskaya, Surf. Sci. **523**, 211 (2003).
13. J. Kim, M. C. Gallagher, and R. F. Willis, Appl. Surf. Sci. **67**, 286 (1993).
14. I. M. Vitomirov, A. Raisanen, A. C. Finnefrock, *et al.*, Phys. Rev. B **46**, 13293 (1992).
15. W. Mönch, *Semiconductor Surfaces and Interfaces* (Springer, Berlin, 1993).
16. M. D. Pashley, Phys. Rev. B **40**, 10481 (1989).
17. S. Moré, S. Tanaka, S. Tanaka, *et al.*, Surf. Sci. **454–456**, 161 (2000).
18. T. Kendelewicz, P. Soukiassian, M. H. Bakshi, *et al.*, Phys. Rev. B **38**, 7568 (1988).

Translated by A. Bagatur'yants

Aharonov–Bohm Oscillation Amplitude in Small Ballistic Interferometers

V. A. Tkachenko^{1,*}, Z. D. Kvon^{1,2}, D. V. Sheglov^{1,2}, A. V. Latyshev^{1,2}, A. I. Toropov¹,
O. A. Tkachenko^{1,2}, D. G. Baksheyev¹, and A. L. Aseev¹

¹ *Institute of Semiconductor Physics, Siberian Division, Russian Academy of Sciences, Novosibirsk, 630090 Russia*

* e-mail: vtkach@isp.nsc.ru

² *Novosibirsk State University, Novosibirsk, 630090 Russia*

Received January 8, 2004

Small-radius (110 nm) ring interferometers were fabricated by the local anodic oxidation of AlGaAs/GaAs heterostructures containing 2D electron gas. Measurements and modeling show that a small ring asymmetry, which is detected by an atomic force microscope, leads to a small amplitude of Aharonov–Bohm oscillations, while a stronger asymmetry completely suppresses these oscillations. © 2004 MAIK “Nauka/Interperiodica”.

PACS numbers: 73.23.Ad; 73.20.-r; 73.50.-h

The properties of ring electron interferometers have been studied for twenty years, starting with pioneering publications [1]. Owing to the Aharonov–Bohm (AB) effect, these devices most clearly demonstrate the effect of quantum interference on electric resistance. The period of AB oscillations in a magnetic field is a stable parameter characterizing each individual interferometer; it is determined by the ratio of the magnetic flux quantum h/e to the ring area. The AB oscillation amplitude was found to be much less stable and unexpectedly small in many experiments. Previous studies mainly dealt with ballistic ring interferometers fabricated by electron lithography and subsequent plasma chemical etching of AlGaAs/GaAs heterostructures containing high-mobility 2D electron gas [2]. This technique allowed the fabrication of ring interferometers of a rather small size ($r = 130$ nm) and the observation of AB oscillations at temperatures up to 4.2 K [3]. However, the reasons why the AB oscillation amplitude is often found to be much smaller than expected remained unexplained.

Recently, it has become possible to fabricate interferometers using the oxidation of the heterostructure surface by the tip of an atomic force microscope (AFM) [4, 5]. This technique makes it possible to obtain even smaller interferometers and control the geometry of the structure with a higher accuracy. It is significant that, with the AFM technique, one obtains a detailed image of the surface relief for each sample, and it can be compared with the results of transport measurements. Basically, this gives one the chance to study experimentally the effect of the actual ring topology on the amplitude of AB oscillations. In addition, using the sample images, one can model electrostatic properties of the devices under consideration [6, 7] and their conductance [6–8]. As a result, a more detailed comparison

becomes possible between the theory of semiconductor ballistic structures and the corresponding experimental data.

This paper describes the study of ring interferometers fabricated using the AFM technique and characterized by an effective radius of $r = 110$ nm. As an initial structure with 2D electron gas, AlGaAs/GaAs heterojunctions with a small distance (25 nm) between the 2D electron gas and the surface were grown. The mobility of 2D electron gas was $\mu = 10^5$ cm²/(V s) at an electron concentration of $N_s = 5 \times 10^{11}$ cm⁻², and the corresponding electron mean free path was $l = 1.2$ μm. The ring fabrication procedure was as follows. Preliminarily, using a Solver P-47H (NT-MDT) atomic force microscope, the surface morphology of the initial heterojunction was studied in the semicontact scanning mode. After the information on the surface area of interest had been obtained, the local anodic oxidation process was initiated [5, 9]. The oxidation was performed using a specially manufactured template in the scanning mode of surface modification. At the points marked on the template, an electric potential, negative with respect to the surface, was applied to the AFM probe to initiate the local anodic oxidation processes at these points. The intensity of the oxidation process was controlled by the magnitude of the probe–sample voltage. The geometric dimensions of the oxidized patches were determined by the time of applying the oxidizing voltage and by the relative air humidity. To obtain a deeper surface modification, the system of voltage feed to the AFM probe was improved so as to obtain probe–sample voltages up to 40 ± 0.2 V and a total oxide thickness up to 50 nm. For structures shown in Fig. 1, the oxidizing potential was ~ 20 V. This provided a height of ~ 12 nm for the local anodic oxidation line at a relative humidity of 40%. The AFM images and the surface modification

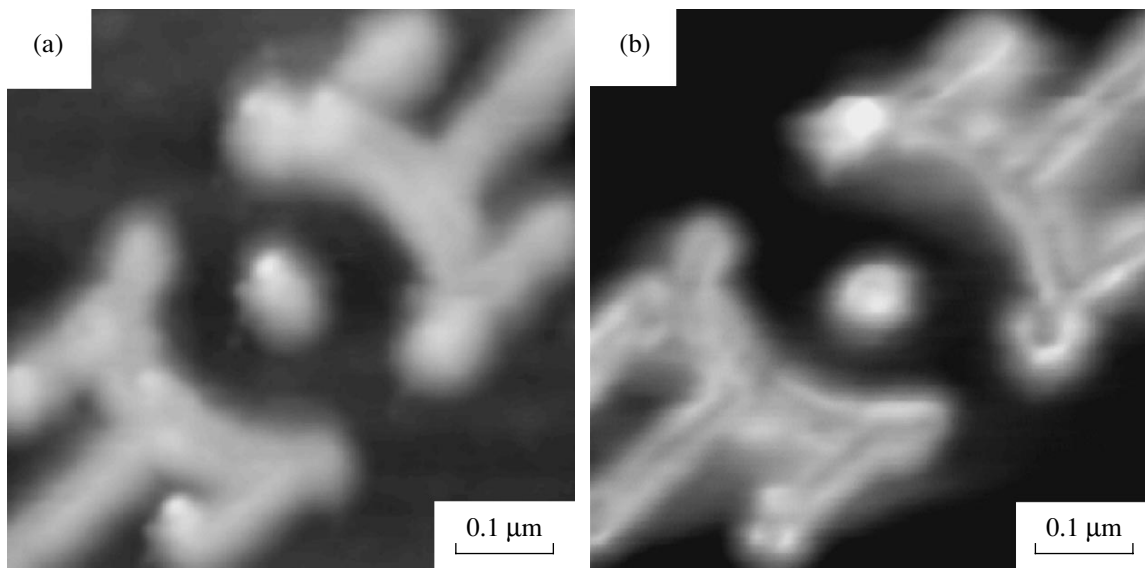


Fig. 1. AFM images of open rings fabricated by the local anodic oxidation technique: (a) symmetric and (b) asymmetric rings.

were obtained in the resonance semicontact mode with the use of standard cantilevers ($\nu = 150$ kHz). One can see from Fig. 1 that the line height and width vary from point to point and from sample to sample; i.e., the geometry preset by the template is randomly disturbed. The image of one of the rings (“symmetric” ring) is shown in Fig. 1a. Next to it, another (“asymmetric”) ring is shown; the arms forming this ring have different widths (Fig. 1b). It should be noted that we present the images of the rings studied in the experiment rather than of the reference samples, for which no transport measurements are usually carried out [7]. Thus, in contrast to the standard technology, we can directly study the resistance response to small deviations from the ideal geometry that occur upon the fabrication of nanostructures near the limit of lithography resolving power.

The resistance of the aforementioned rings was measured in the temperature range 1.5–4 K in magnetic fields up to 1 T. The results of these measurements at 3.3 K are shown in the left panel in Fig. 2. One can clearly see that the curve obtained for the symmetric ring (curve *a*) exhibits AB oscillations. The subtraction of the background reveals the presence of beats in the oscillations of the quantity δR . The oscillation amplitude reaches 5%. Note that, upon a further decrease in temperature, the maximal oscillation amplitude remained virtually unchanged. The AB effect persisted for different cooling cycles and illuminations of the sample, although the background resistance varied considerably (e.g., by a factor of two). The right panel in Fig. 2 shows the Fourier spectrum of AB oscillations that was obtained by averaging over several curves $\delta R(B)$ for the symmetric ring. The spectrum consists of a single narrow peak corresponding to the oscillation period $\Delta B = 0.11$ T in a magnetic field. This period cor-

responds to the ring effective radius $r = 110$ nm. Note that no publications reporting such a small ring interferometer obtained by local anodic oxidation are available to us.

The results obtained for the asymmetric ring are also shown in Fig. 2 (curve *b*). No oscillations, at least none exceeding 0.1%, are observed in this case. Other cooling cycles and illuminations also revealed no oscillations for this sample, although the curve shapes and the zero-field resistance varied. Thus, a fundamental distinction is observed in the behavior of the rings under

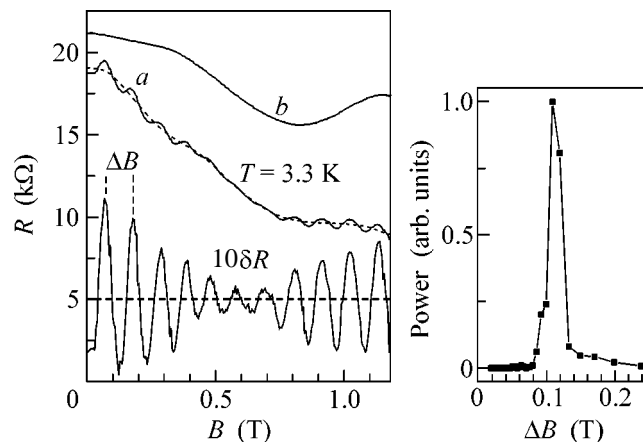


Fig. 2. The left panel presents the measured magnetic field dependence of the resistance for the samples shown in Fig. 1: (a) symmetric and (b) asymmetric rings; the lower curve represents the quantity $\delta R = R - \langle R \rangle$ for the symmetric ring. The right panel presents the Fourier spectrum of the dependences $\delta R(B)$ for the symmetric ring.

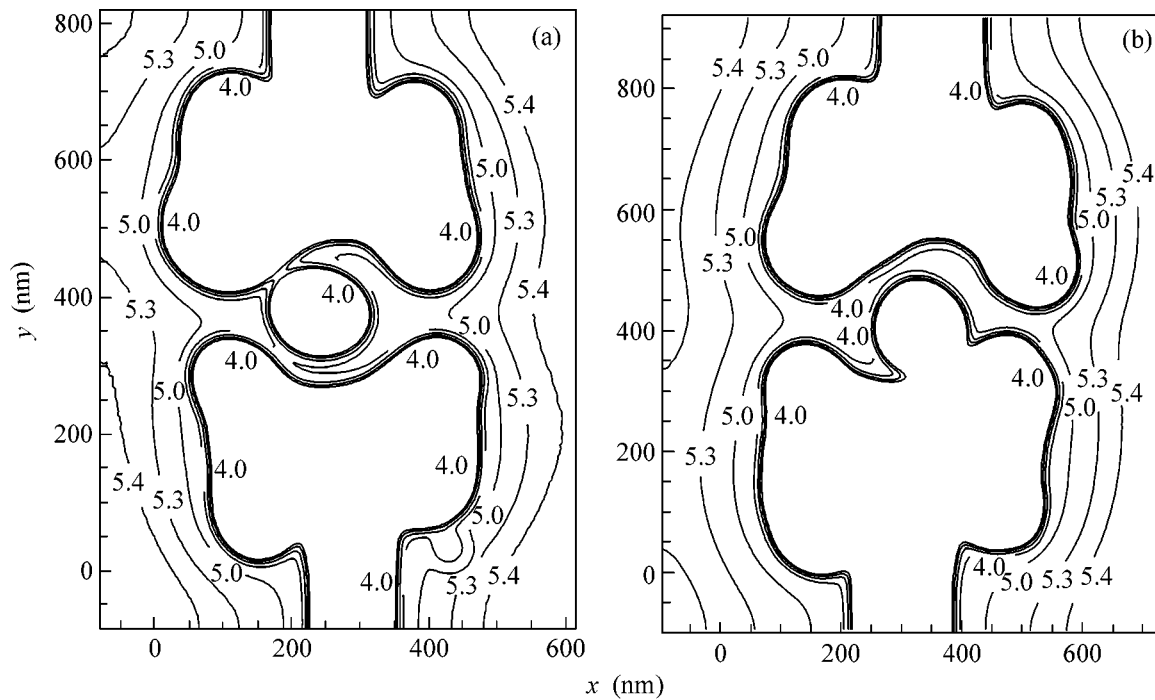


Fig. 3. Calculated 2D electron density distribution for the (a) symmetric and (b) asymmetric rings shown in Fig. 1 (isolines in units of 10^{11} cm^{-2}).

study. The symmetric ring exhibits the AB effect, testifying to the interference associated with the electron transport through the two ring arms [1]. In the asymmetric ring, no traces of such an interference were observed. The behavior of the rings was found to be stable to changes in the fluctuation potential as a result of recharging impurities. This fact suggests that the presence or absence of the AB oscillations is determined by the difference in the geometry of the electron rings.

In this study, the aforementioned assumption was verified by modeling the electrostatic properties of the rings and their resistance with allowance made for all actual parameters of the structures under investigation. The methods of calculation are similar to those described in [6, 7], but, in our case, we took into account the complicated dependence of the oxidation line height h on the position of a point on the plane. One of the boundary conditions used in solving the three-dimensional Poisson equation was determined from the 2D distribution of the depth H to which oxide penetrates into the semiconductor. At the semiconductor-oxide boundary, we used the condition for pinning the Fermi level by the surface states lying at the center of the GaAs band gap. It was assumed that H is proportional to the measured quantity h . For these conditions, we verified the applicability of the known proportionality coefficient for the GaAs structures ($H/h \approx 1.5$ [5]) to our case. The calculation showed that, with this value, both electron rings are broken and cannot exhibit AB oscillations. For the modeling to be adequate to the

experimental situation, it is necessary to reduce the value of H/h to 1.2. It should be noted that the small values $H < H_0 = 3 \text{ nm}$ were neglected to reduce the effect of the initial surface roughness and the measurement error for h in the ring arms, i.e., in the narrow dips of the relief. In these areas, the measured value of h can be greater than its true value because of the finite thickness of the AFM tip. Microscale inhomogeneities of charge distribution in delta-doped layers (fluctuation potential [7]) were not taken into account to simplify the analysis of the effects associated with the geometry. The results of the self-consistent modeling of the potential and electron density are shown in Figs. 3a (symmetric ring) and 3b (asymmetric ring). One can see that, in the first case, the electron ring is in fact asymmetric but has two conducting arms, whereas, in the second case, the narrower arm is broken by a wide gap. To check whether the model fits the experiment, the zero-field 2D ballistic transport was calculated. The calculation shows that the resistances of the electron systems are close to the resistance quantum $h/2e^2$ and can irregularly vary by approximately $h/4e^2$ with varying Fermi level E_F . This agrees well with the results of measurements and with the observation of the random resistance variations caused by switching the fluctuation potential.

Important information on the asymmetry of the electron rings can be obtained by calculating the subbands $E_n(x)$, i.e., the energy levels of the finite motion across the longitudinal axis of the interferometer. The result of such a calculation for the symmetric ring is

presented in Fig. 4a. The outermost barriers correspond to the ring inputs, and the central barriers, to its arms. The anticrossings of the subbands in the central part of the figure are caused by the abrupt narrowing of the channel in one of the ring arms. When calculating the potential, the Fermi level was taken to be zero. Figure 4a shows that two one-dimensional modes ($1r$, $2r$) are propagated in one of the arms (r), while only one mode ($1l$) is propagated in the other arm (l). One can expect that the AB effect should persist in this case. In the second ring, one of the arms is interrupted by a wide barrier. From the subband picture, it was found that, for the lower mode, the top of this barrier reaches 47 meV above the Fermi level. The calculated penetrability of such a tunneling gap in zero magnetic field is negligibly small (10^{-27}) and remains so when the parameters H/h , H_0 , and E_F are varied within the allowable limits. Naturally, the AB effect is absent in this structure.

The transition from the abovebarrier transport to tunneling, which occurs in the narrowest part of the ring, was modeled by varying E_F in the first ring. The magnetic field dependence of the conductance was calculated by the method of recursive Green's functions [8] for the effective 2D potential obtained from the self-consistent electrostatic calculations. Let V_b denote the barrier height for the $1l$ subband in the narrow part of the ring. From Fig. 4a, it follows that $V_b = -1$ meV. The conductance calculation shows that the AB oscillations have an amplitude of $\sim 10\%$ at $E_F - V_b \approx 1$ meV but are strongly attenuated when the transition to tunneling occurs (Fig. 4b). Therefore, no AB oscillations are possible in the second ring, in which V_b is several tens of millielectronvolts higher than E_F . Interestingly, the asymmetry of the potential in the first ring at $E_F \approx 0$ meV gives an oscillation amplitude close to that observed in the experiment. A good agreement between experiment and theory was obtained without taking into account phase interruption of the electron wave function and without smoothing the curves. Although the actual asymmetry of the potential has never been investigated before, we can assume that our mechanism of suppression of the AB oscillations is operative in many other structures. This hypothesis is indirectly confirmed by the small yield of working samples exhibiting AB oscillations, independently of the fabrication technology.

Concerning the reliability of our modeling, it should be noted that the measured period of AB oscillations is one-third smaller than the calculated period; i.e., the calculated effective area of the ring proves to be smaller than the effective area in the experiment. It is significant that both areas fit into the size of the electron system of the interferometer and, hence, no fundamental disagreement occurs between the theory and experiment. However, the period of AB oscillations, unlike their amplitude, is stable, and the determination of the origin of the difference in the periods calls for further investigation.

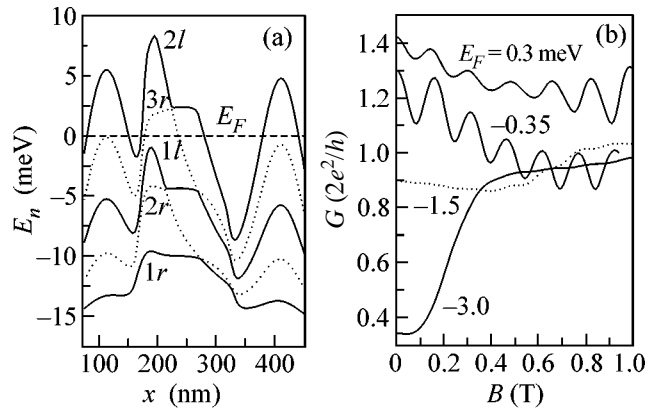


Fig. 4. (a) Quantization spectrum, E_n , in the sections across the x axis for the device shown in Fig. 3a: curves $1r$ – $3r$ refer to the levels in the wider ring arm, and curves $1l$ and $2l$, to the levels in the narrower arm. (b) Calculated magnetic field dependence of the conductance of the same ring for different values of E_F .

Thus, using the probe lithography technique, we fabricated a semiconductor ring interferometer with an effective radius of 110 nm. We found that small errors in the nanolithography may cause a break in the arm of the electron ring and completely suppress the AB oscillations. By both experiment and calculation, we showed that the amplitude of the AB oscillations is small for a ring that is close to being broken. The results of this study and the previous studies suggest that the mechanism we found to be responsible for the suppression of the AB oscillations is rather common.

This work was supported by the Russian Foundation for Basic Research (project no. 16516), the INTAS (project no. 01-0014), the Russian Academy of Sciences (the programs “Quantum Macrophysics” and “Low-Dimensional Quantum Structures”), the Ministry of Industry and Science (the programs “FOKVT,” “FTNS,” and “NMKS”), and the Ministry of Education of the Russian Federation (the program “Integration” and the State Contract no. 40765/785).

REFERENCES

1. M. Büttiker, Y. Imry, and R. Landauer, *Phys. Lett. A* **96A**, 365 (1983); M. Büttiker, Y. Imry, and M. Ya. Azbel, *Phys. Rev. A* **30**, 1982 (1984).
2. G. Timp, A. M. Chang, J. E. Cunningham, *et al.*, *Phys. Rev. Lett.* **58**, 2814 (1987); C. J. B. Ford, A. B. Fowler, J. M. Hong, *et al.*, *Surf. Sci.* **229**, 307 (1990); K. Ismail, S. Washburn, and K. Y. Lee, *Appl. Phys. Lett.* **59**, 1998 (1991); A. A. Bykov, Z. D. Kvon, E. B. Ol’shanetskiĭ, *et al.*, *Pis'ma Zh. Éksp. Teor. Fiz.* **57**, 596 (1993) [*JETP Lett.* **57**, 613 (1993)]; M. Casse, Z. D. Kvon, G. M. Gusev, *et al.*, *Phys. Rev. B* **62**, 2624 (2000).

3. A. A. Bykov, D. G. Baksheev, L. V. Litvin, *et al.*, Pis'ma Zh. Éksp. Teor. Fiz. **71**, 631 (2000) [JETP Lett. **71**, 434 (2000)].
4. A. Fuhrer, S. Lüsher, T. Ihn, *et al.*, Nature **413**, 822 (2001); U. F. Keyser, S. Bock, R. J. Haug, *et al.*, Semicond. Sci. Technol. **17**, L22 (2002).
5. R. Held, T. Vancura, T. Heizel, and K. Ensslin, Appl. Phys. Lett. **73**, 262 (1998).
6. O. A. Tkachenko, V. A. Tkachenko, D. G. Baksheev, *et al.*, Pis'ma Zh. Éksp. Teor. Fiz. **71**, 366 (2000) [JETP Lett. **71**, 255 (2000)].
7. V. A. Tkachenko, A. A. Bykov, D. G. Baksheev, *et al.*, Zh. Éksp. Teor. Fiz. **124**, 351 (2003) [JETP **97**, 317 (2003)].
8. T. Ando, Phys. Rev. B **44**, 8017 (1991).
9. D. V. Sheglov, A. V. Prozorov, D. A. Nasimov, *et al.*, Phys. Low-Dimens. Semicond. Struct. **5–6**, 239 (2002).

Translated by E. Golyamina